

# A Heteroclinic Connection between Two Saddle Slow Manifolds in the Olsen Model

Elle Musoke, Bernd Krauskopf, and Hinke M. Osinga

*Department of Mathematics, University of Auckland, Private Bag 92019*

*Auckland, 1142, New Zealand*

*elle.musoke@auckland.ac.nz*

Received (to be inserted by publisher)

The abstract should summarize the context, content and conclusions of the paper. It should not contain any references or displayed equations. Typeset the abstract in 10 pt Times Roman with baselineskip of 12 pt, making an indentation of 1.6 cm on the left and right margins.

*Keywords:* A list of 3–5 keywords are to be supplied.

## 1. Introduction

Multiple-time scale dynamical systems are characterized by certain variables evolving on a fast time scale while other variables evolve on a slower time scale. The separation of variables into fast and slow can be found in many systems: chemical systems, neurons, electric circuits, lasers, and predator-prey dynamics, among others, have been described by slow-fast models [Brøns & Bar-Eli, 1991; De Maesschalck & Wechselberger, 2015; Van der Pol, 1927; Otto *et al.*, 2012; Piltz *et al.*, 2017]. In [Brøns & Bar-Eli, 1991], oscillations in the Belousov-Zhabotinsky reaction arise as a consequence of time-scale splitting. Slow-fast models for neurons are studied in [De Maesschalck & Wechselberger, 2015] in which different time scales result in neural excitability. One of the most famous slow-fast systems is presented in [Van der Pol, 1927] in which time-scale splitting again causes oscillations in a circuit. Lasers can also be modelled with slow-fast systems as shown in [Otto *et al.*, 2012] which investigated interspike interval length. A more ecological example can be found in [Piltz *et al.*, 2017] which uses a slow-fast model to investigate the effect of a changing predator diet on predator-prey dynamics. By reason of their ubiquity, various phenomena that arise from the multiple-time-scale nature of slow-fast systems are of significant interest. These have been described for two- and three-dimensional systems by well-established theory [Benoît *et al.*, 1981; Benoît, 1982, 1985; Guckenheimer, 1985; Brøns *et al.*, 2006; Krupa *et al.*, 2008].

We are concerned here with mechanisms responsible for the oscillatory behaviours exhibited by many slow-fast systems. In two-dimensional systems canard explosions, small-amplitude limit cycles transitioning to larger-amplitude relaxation oscillations were studied, for example, in the Van der Pol oscillator and the FitzHugh–Nagumo model [Benoît *et al.*, 1981; FitzHugh, 1955]. In three-dimensional systems, periodic orbits (POs) with epochs of localized small-amplitude oscillations (SAOs) and epochs of large-amplitude oscillations (LAOs) have been observed [Hudson *et al.*, 1979]. The mechanisms that cause SAOs of these appropriately named mixed-mode oscillations (MMOs) are described in [Desroches *et al.*, 2012] for three-dimensional systems. In this paper, we investigate novel phenomena that arise in four-dimensional slow-fast systems which may provide insight into undiscovered mechanisms for MMOs in higher-dimensional systems.

Previous studies exploring the mechanisms for MMOs in slow-fast dynamical systems investigate the role of so-called slow manifolds in the MMOs' generation and organisation [Vo *et al.*, 2013a,b; Harvey *et al.*, 2010; Mitry *et al.*, 2013; Hasan *et al.*, 2018]. Slow manifolds are families of trajectories on which the flow evolves on the slow timescale. A slow manifold may have families of trajectories that converge toward it in forward or backward time, respectively called the stable and unstable manifolds of the slow manifold. Slow manifolds may have both a stable and an unstable manifold in which case we say it is a saddle slow manifold.

Literature concerning slow manifolds explores slow manifolds and systems of, respectively, varying dimensions. Endocrine pituitary cells were studied with a four-dimensional slow-fast model that had a two-dimensional slow manifold in [Vo *et al.*, 2013b]. In [Harvey *et al.*, 2010] a three-dimensional slow manifold was studied in a four-dimensional model for calcium oscillations inside cells. In [Vo *et al.*, 2013a] a four-dimensional model for a pituitary lactotrophic cell was investigated from both a two- and three-timescale viewpoints. From the two-timescale perspective, the model has a three-dimensional slow manifold. In [Mitry *et al.*, 2013] a six-dimensional model for an excitable neuron was investigated. The model had a two-dimensional slow manifold which plays a role in the generation of oscillations in the system. A five-dimensional model with a one-dimensional slow manifold was also investigated. In [Farjami *et al.*, 2018] techniques were developed to compute stable and unstable manifolds of one-dimensional saddle slow manifolds in three-dimensional systems. In [Hasan *et al.*, 2018], these techniques were generalised to compute a two-dimensional saddle slow manifold and its two-dimensional stable and unstable manifolds in the four-dimensional Hodgkin–Huxley model. To our knowledge, there is no literature on the computation of three-dimensional (un)stable manifolds of one-dimensional saddle slow manifolds at this time.

We consider a prototypical four-dimensional slow-fast dynamical system that exhibits MMOs, namely an Olsen model for peroxidase-oxidase reaction. First introduced by Lars F. Olsen in 1983 [Olsen, 1983], there are currently many different versions of the Olsen model of different dimensions. We consider the Olsen model in the form from [Kuehn & Szmolyan, 2015] and earlier work. The MMO  $\Gamma$  in the Olsen model phase space is of particular interest because it does not seem to be generated by the mechanisms for MMOs familiar from three-dimensional systems.

The classification of variables into those that evolve on a fast time scale and those that evolve on a slow time scale is not straightforward for the Olsen model because the variables are not consistently slow or fast over all regions of phase space. In fact, the Olsen model nominally has three different time scales. We focus specifically on a parameter regime corresponding to two different time scales with three fast and one slow variables. This parameter regime also corresponds to attracting  $\Gamma$  and was the focus in [Desroches *et al.*, 2009]. This study reported on mechanisms for  $\Gamma$  after a model reduction to a three-dimensional system. Two saddle slow manifolds were computed along with their stable and unstable manifolds. These gave insight into the formation of the Olsen model MMO, as well as the cause of its particular geometry. However, because of the assumptions used to reduce the model to a three-dimensional system, the dimensions of the stable manifold of one slow manifold and unstable manifold of the other were reduced to two in contrast to the corresponding three-dimensional manifolds in the full system.

Examples of computing and visualising three-dimensional manifolds are in [Waalkens *et al.*, 2005; H\'aro & de la Liave, 2006; Jorba & Olmedo, 2009]. None of these examples are in the context of computing (un)stable manifolds of saddle slow manifolds. Tools to implement the computation of three-dimensional manifolds are not widely used at this time and, once computed, it is difficult to see the dynamics on the manifold in lower-dimensional projections. Due to the nature of the current computation tools available, computing the entire three-dimensional manifold would also be computationally expensive compared to the computation of two-dimensional manifolds.

In the full system, the three-dimensional stable manifold of one slow manifold and the three-dimensional unstable manifold of the other are expected to intersect generically in a two-dimensional surface of connections between the two slow manifolds. Such a surface does not generically exist in four-dimensional systems for slow manifolds of dimension greater than one. The surface of connections also does not exist generically in systems of dimension lower than four. In these cases, the stable and unstable manifolds of the saddle slow manifolds are limited to dimensions of two or lower and therefore do not typically have robust intersections of dimension two or higher. In this research, we generalise the techniques in [Farjami

[*et al.*, 2018] with the aim of computing the three-dimensional stable and unstable manifolds of the one-dimensional saddle slow manifolds in the Olsen model. Furthermore, we use our techniques in conjunction with Lin’s method to compute the intersection of the three-dimensional stable and unstable manifolds in the full four-dimensional model. This intersection is involved in the formation and organisation of  $\Gamma$  and could lead to insights about the formation and organisation of MMOs in other higher-dimensional systems.

This paper is organized as follows. In the next section we give the necessary background from geometric singular perturbation theory (GPST) for defining the three-dimensional manifolds which are the focus of this research. Section 3 gives definitions of the manifolds which are then computed. In section 4, a computation of the intersection of the manifolds from section 3 is described for the case where the time-scaling parameter is greater than zero as well as for the case when the time-scaling parameter is equal to zero. Section 5 gives an analysis of differences between the manifolds computed in section 4. Conclusions are given in section 6.

## 2. The Olsen Model

We consider the scaled system from [Kuehn & Szmolyan, 2015], given as the system of ordinary differential equations

$$\begin{cases} \frac{dA}{dt} = \mu - \alpha A - ABY, \\ \frac{dB}{dt} = \varepsilon(1 - BX - ABY), \\ \frac{dX}{dt} = \lambda(BX - X^2 + 3ABY - \zeta X + \delta), \\ \frac{dY}{dt} = \kappa\lambda(X^2 - Y - ABY), \end{cases} \quad (1)$$

where  $(A, B, X, Y) \in \mathbb{R}^4$  are positive concentrations of chemicals. The system parameters are represented by the Greek letters appearing in (1) and these have the values given in Table 1. With the minor modification, for notational convenience, of using  $\varepsilon$  for  $\varepsilon_b$  and  $\frac{1}{\lambda}$  for  $\varepsilon^2$ , they are chosen to be as in [Kuehn & Szmolyan, 2015]. The time-scaling parameters  $\varepsilon$  and  $\lambda$  are chosen so that we are dealing with a regime with three fast variables,  $A$ ,  $X$ , and  $Y$ , and one slow variable,  $B$ .

Table 1. Parameters of system (1) as in [Kuehn & Szmolyan, 2015] so that  $A$ ,  $X$ , and  $Y$  are fast and  $B$  is slow.

$\alpha$	$\delta$	$\varepsilon$	$\lambda$	$\kappa$	$\mu$	$\zeta$
0.0912	$1.2121 \times 10^{-4}$	0.0037	18.5281	3.7963	0.9697	0.9847

The classical analysis of slow-fast systems considers the two singular limits, for example, [Desroches *et al.*, 2012]. In the limit of  $\varepsilon = 0$ , system (1) reduces to

$$\begin{cases} \frac{dA}{dt} = \mu - \alpha A - ABY, \\ \frac{dX}{dt} = \lambda(BX - X^2 + 3ABY - \zeta X + \delta), \\ \frac{dY}{dt} = \kappa\lambda(X^2 - Y - ABY), \end{cases} \quad (2)$$

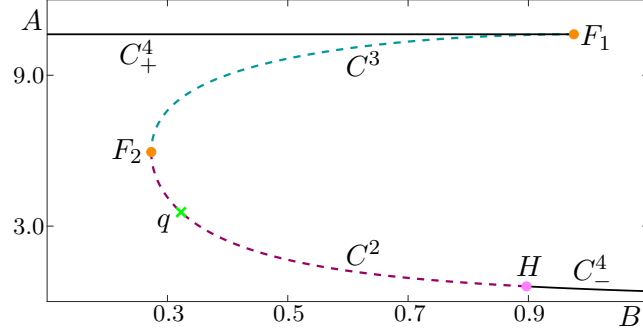


Fig. 1. Physically relevant branches  $C^2$ ,  $C^3$ ,  $C_{\pm}^4$  of the critical manifold of (1) shown in projection onto the  $(B, A)$ -plane. Branches  $C^2$  (dashed, red curve) and  $C^3$  (dashed, blue curve) consist of saddles of (2) and  $C_{\pm}^4$  (solid, black curves) consist of attractors of (2). Superscripts indicate the dimension of the stable eigenspace of the branch and subscripts are used to distinguish between the two branches of attractors. Branches are divided by saddle-node bifurcation points  $F_1$  and  $F_2$  (orange dots) and a Hopf point  $H$  (pink dot). Also shown is a saddle equilibrium  $q$  (green cross) of (1) existing on  $C^2$ . Parameters are as in Table 1.

with  $\frac{dB}{dt} = 0$ , meaning that  $B$  is a parameter of (2). We refer to the three-dimensional system (2) as the fast subsystem. Performing the time rescaling  $\tau = \varepsilon t$  and then considering the limit of  $\varepsilon = 0$ , system (1) reduces to the differential algebraic reduced system

$$\begin{cases} 0 &= \mu - \alpha A - ABY, \\ \frac{dB}{d\tau} &= (1 - BX - ABY), \\ 0 &= \lambda(BX - X^2 + 3ABY - \zeta X + \delta), \\ 0 &= \kappa\lambda(X^2 - Y - ABY). \end{cases} \quad (3)$$

The three algebraic equations in system (3) define a one-dimensional manifold, called the critical manifold, denoted  $C$ .

The critical manifold  $C$  consists of equilibria of the fast subsystem (2), which exist in  $(A, B, X, Y)$ -space for different values of  $B$ . Their stability can be determined from the eigenvalues of the  $3 \times 3$  Jacobian matrix of (2) evaluated at each point on the critical manifold. Points  $p \in C$  at which the Jacobian of (2) has eigenvalues with non-zero real parts are called hyperbolic. The eigenvectors associated with the eigenvalues are categorized based on the sign of the real part of the associated eigenvalue. Eigenvectors whose associated eigenvalues have negative real parts are called stable directions of  $p$  and these span the stable eigenspace  $E^s(p)$  of  $p$ . The unstable directions and the unstable eigenspace,  $E^u(p)$ , can be defined similarly by the eigenvectors associated with eigenvalues having positive real part. Note that the dimensions of the stable and unstable eigenspaces are equal to the number of eigenvalues with negative and positive real parts respectively. Equilibria at which the Jacobian has eigenvalues with zero real-part are called non-hyperbolic and these correspond to bifurcations of system (2) [Kuznetsov, 2009].

The critical manifold  $C$  in  $(A, B, X, Y)$ -space is divided into branches by bifurcation points of the fast subsystem (2), so that points on each branch have the same dimensions of stable and unstable eigenspaces. In other words, the branches of  $C$  are one-parameter families in  $B$  of hyperbolic equilibria of system (2). We define the stable eigenspace  $E^s(C^i)$  of a branch  $C^i$  as the collection of stable eigenspaces of all the points on the branch. The dimension of  $E^s(C^i)$ , hence, one plus than the dimension of the stable eigenspace of each point on the branch. In our notation for branches, superscripts indicate the dimension in  $(A, B, X, Y)$ -space of the stable eigenspace of the branch. Further, we use subscripts to distinguish the two branches on which equilibria have three-dimensional stable eigenspaces, that is, are attracting.

Four branches of  $C$  lie in the physically relevant region where all phase-space variables are positive,

these are shown in Figure 1 in projection onto the  $(B, A)$ -plane. The uppermost branch denoted  $C_+^4$  (solid, black curve) consists of stable equilibria of (2). It is separated from the branch of saddle equilibria denoted  $C^3$  (dashed, teal curve), by a very sharp fold at the point  $F_1$  (orange dot) at  $B \approx 0.956$ . Folds of the critical manifold correspond to saddle-node bifurcations of system (2) with respect to the parameter  $B$ , these are points at which one of the real eigenvalues of the Jacobian evaluated at the point changes signs. Another fold at  $B \approx 0.273$  denoted  $F_2$  (orange dot), separates  $C^3$  from a lower branch of saddle equilibria denoted  $C^2$  (dashed, raspberry curve). The branch  $C^2$  ends at a Hopf bifurcation  $H$  (pink dot) at  $B \approx 0.897$ , where two complex-conjugate eigenvalues of the Jacobian pass through the imaginary axis of the complex plane. To the right of  $H$ , there is again a stable branch of equilibria denoted  $C_-^4$  (solid, black curve).

The point  $q$  (green cross) on  $C^2$  at  $B \approx 0.323$  is an equilibrium of system (3) and is, hence, an equilibrium for the full system (1). The equilibrium  $q$  has a two-dimensional stable and two-dimensional unstable manifold, denoted  $W^s(q)$  and  $W^u(q)$ , respectively. The manifolds  $W^s(q)$  and  $W^u(q)$  consist of trajectories in  $(A, B, X, Y)$ -space that converge to  $q$  in forward and backward time respectively. To the right of  $W^u(q)$ , in the  $(B, A)$ -projection, the flow is from right to left near  $C^2$ . To the left of  $W^u(q)$ , in the  $(B, A)$ -projection, the flow is from left to right near  $C^2$ . The manifolds  $W^s(q)$  and  $W^u(q)$  can be computed with the methods in [Krauskopf *et al.*, 2007]; They are not depicted in Figure 1, but are shown in Figure 10.

Our interest is in the branches  $C^3$  and  $C^2$  because they are saddle objects of different type and are crucial for organising the phase space. These branches of the critical manifold are invariant for  $\varepsilon = 0$ , but not for  $\varepsilon > 0$ . However, they do persist as locally invariant manifolds called slow manifolds [Fenichel, 1979]. The associated slow manifolds are traditionally denoted  $S_\varepsilon^3$  and  $S_\varepsilon^2$  but, for notational convenience, we drop the subscript indicating dependence on  $\varepsilon$  and refer to these slow manifolds for  $\varepsilon > 0$  simply as  $S^3$  and  $S^2$ . The slow manifold  $S^3$  has the same dimension and stability and lies at an  $O(\varepsilon)$  Hausdorff distance from  $C^3$ . In particular,  $S^3$  converges to  $C^3$  as  $\varepsilon \rightarrow 0$ . (For a definition of Hausdorff distance see, e.g., [Rockafellar & Wets, 2009].) Orbit segments that lie on a slow manifold remain slow for  $O(1)$  time with respect to the slow time scale. It follows that any trajectory that remains slow for an  $O(1)$  amount of slow time can be considered (to be on) a slow manifold. However, eventually trajectories on a slow manifold may become fast. Due to their finite time nature, slow manifolds are not unique; however, any two slow manifolds lie exponentially close to each other in a suitable  $O(\varepsilon)$  neighbourhood of  $C$  [Fenichel, 1979]. To select unique representatives  $S^3$  and  $S^2$ , we consider the slow manifold that remains slow for the longest amount of time in a specific numerical setup in section 3.

The Stable Manifold Theorem tells us that each  $p \in C^3$  has a stable and an unstable manifold that are tangent to and have the same dimensions as  $E^s(p)$  and  $E^u(p)$ , respectively. We denote the stable manifold of a point  $p \in C^3$  by  $W^s(p)$  and its unstable manifold by  $W^u(p)$ . We can then define the collection of stable manifolds for  $p \in C^3$  as  $W^s(C^3) = \bigcup_{p \in C^3} W^s(p)$ , which is a three-dimensional manifold tangent to  $E^s(C^3)$ . We can similarly define the three-dimensional unstable manifold  $W^u(C^2)$  of  $C^2$  which is tangent to  $E^u(C^2)$ .

According to Fenichel Theory, for  $\varepsilon > 0$ , the manifold  $W^s(C^3)$  also persists in an  $O(\varepsilon)$  neighbourhood as a three-dimensional local stable manifold  $W_{loc}^s(S^3)$  of  $S^3$ . The local stable manifold  $W_{loc}^s(S^3)$  consists of families of trajectories that have a fast approach to  $S^3$  then remain close to  $S^3$  for  $O(1)$  slow time. The global stable manifold  $W^s(S^3)$  can be obtained by extending  $W_{loc}^s(S^3)$  backwards in time. The three-dimensional unstable manifold  $W^u(S^2)$  associated with  $S^2$  is similarly defined for backwards time. Again, due to the finite-time nature of the definitions for the three-dimensional manifolds  $W^s(S^3)$  and  $W^u(S^2)$ , they are not unique. To select unique representatives, we consider two-parameter families of orbit segments that remain slow for the longest amount of time subject to boundary conditions described in further sections.

### 3. Computation of saddle slow manifolds and their (un)stable manifolds

In [Farjami *et al.*, 2018] algorithms are presented for the computation of a one-dimensional saddle slow manifold and its (un)stable manifolds in a three-dimensional system. We build on their work to define and compute unique representatives  $S^3$  and  $S^2$  as well as their stable and unstable manifolds, respectively.

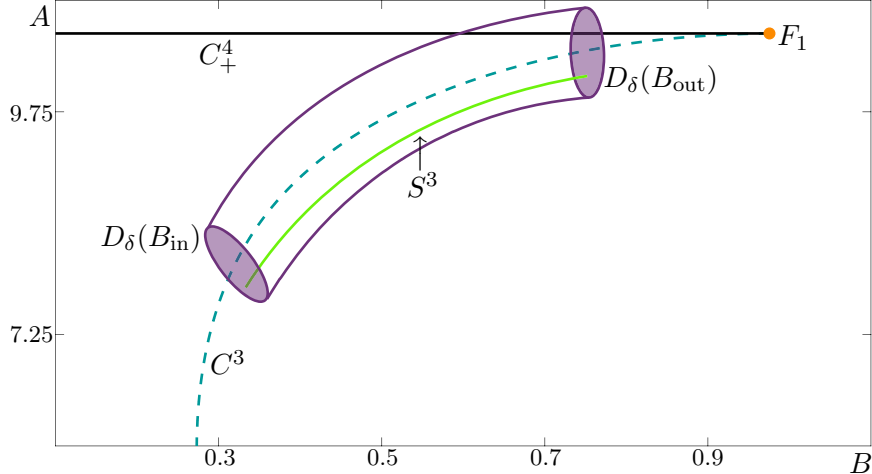


Fig. 2. A sketch of the unique representative slow manifold  $S^3$  (green curve) projected into the  $(B, A)$ -plane. The representative slow manifold  $S^3$  is defined by having the longest integration time while entering and exiting  $D_\delta(B_{\text{in}})$  and  $D_\delta(B_{\text{out}})$  (purple disks) at either end of a four-dimensional cylinder. Also shown are  $C^3$ ,  $C^4_+$ , and  $F_1$ .

### 3.1. Definition of $S^3$

We define the slow manifold  $S^3$  with respect to a closed interval  $[B_{\text{in}}, B_{\text{out}}]$  for the slow variable  $B$ . The values for  $B_{\text{in}}$  and  $B_{\text{out}}$  are chosen such that  $[B_{\text{in}}, B_{\text{out}}] \subset (B_{F_1}, B_{F_2})$ , where  $B_{F_1}$  and  $B_{F_2}$  are the  $B$ -values of the fold points  $F_1$  and  $F_2$ , respectively. Hence, for each  $B_p \in [B_{\text{in}}, B_{\text{out}}]$  there is a unique point  $p = (p_A, p_B, p_X, p_Y) \in C^3$  such that  $p_B = B_p$ . In the three-dimensional subsection  $\{\omega \in \mathbb{R}^4 \mid \omega_B = B_p\}$  we define a solid three-sphere  $D_\delta(B_p)$  with radius  $\delta$  and centre  $p$ , given formally by

$$D_\delta(B_p) = \{w \in \mathbb{R}^4 \mid w_B = B_p, \|w - p\| \leq \delta\}.$$

The union

$$\mathcal{D} = \bigcup_{B_p \in [B_{\text{in}}, B_{\text{out}}]} D_\delta(B_p)$$

forms a four-dimensional compact cylinder. The radius  $\delta$  is small, but it needs to be at least of  $O(\varepsilon)$  to ensure that  $S^3$  lies in  $\mathcal{D}$ . The one-parameter family of orbit segments that enter  $\mathcal{D}$  via  $D_\delta(B_{\text{in}})$  are candidates for  $S^3$ . To select a unique representative  $S^3$  we require that the orbit segment representing  $S^3$  has maximal integration time in  $\mathcal{D}$  while satisfying appropriate boundary conditions. Our choice of boundary conditions is explained in section 3.2.

Figure 2 illustrates this definition with an enlargement of the critical manifold. This is an enlargement of Figure 1 near the branch  $C^3$  where we now sketch the relevant elements of this definition. The unique representative  $S^3$  (represented by a green curve), in projection onto the  $(B, A)$ -plane, enters  $\mathcal{D}$  (represented by purple curves) at  $D_\delta(B_{\text{in}})$  (purple disk) and exits at  $D_\delta(B_{\text{out}})$  (purple disk).

### 3.2. Computation of $W^s(S^3)$ and $S^3$

As  $W^s(S^3)$  is three dimensional it is challenging to compute and difficult to visualise. In fact,  $W^s(S^3)$  can be represented as a two-parameter family of orbit segments that enter  $\mathcal{D}$  at  $D_\delta(B_p)$  for some  $B_p \in [B_{\text{in}}, B_{\text{out}}]$ , and remain inside  $\mathcal{D}$  for  $O(1)$  slow time. A natural way forward is to consider a submanifold of  $W^s(S^3)$  given as a one-parameter family of two-dimensional submanifolds. These can be computed by generalizing the approach in [Farjami *et al.*, 2018], which can then be implemented in the two-point boundary value problem (2PBVP) continuation package AUTO [Doedel, 2007].

Similarly to  $S^3$ , we select and approximate a specific candidate for  $W^s(S^3)$  by requiring that each orbit segment lying on  $W^s(S^3)$  have maximal integration time inside  $\mathcal{D}$  and satisfy appropriate boundary

conditions. We now turn to the computation of the three-dimensional manifold  $W^s(S^3)$  in the region where a corresponding two-dimensional stable manifold was investigated in the reduced model in [Desroches *et al.*, 2009].

To define a submanifold we first define a two-dimensional plane  $\Sigma$  that is transverse to the flow and  $E^u(C^3)$ . We can define  $\Sigma$  by fixing  $A$  and either  $X$  or  $Y$ . A smooth, one-parameter family of solutions of (1) is then given by the property that they begin in  $\Sigma$ , enter  $\mathcal{D}$  at  $D_\delta(B_p)$  for some  $B_p \in [B_{\text{in}}, B_{\text{out}}]$ , and remain inside  $\mathcal{D}$  for  $O(1)$  slow time. We use  $W_\Sigma^s$  to denote the collection of those parts of these orbit segments that enter  $\mathcal{D}$  in the fast direction. The later parts that evolve mostly in the  $B$ -direction inside  $\mathcal{D}$  for  $O(1)$  slow time are approximate segments of  $S^3$ . If the later part of the orbit segment includes a fast exit from  $\mathcal{D}$ , the fast part is an approximation of an orbit segment lying on the unstable manifold  $W^u(S^3)$  of  $S^3$ .

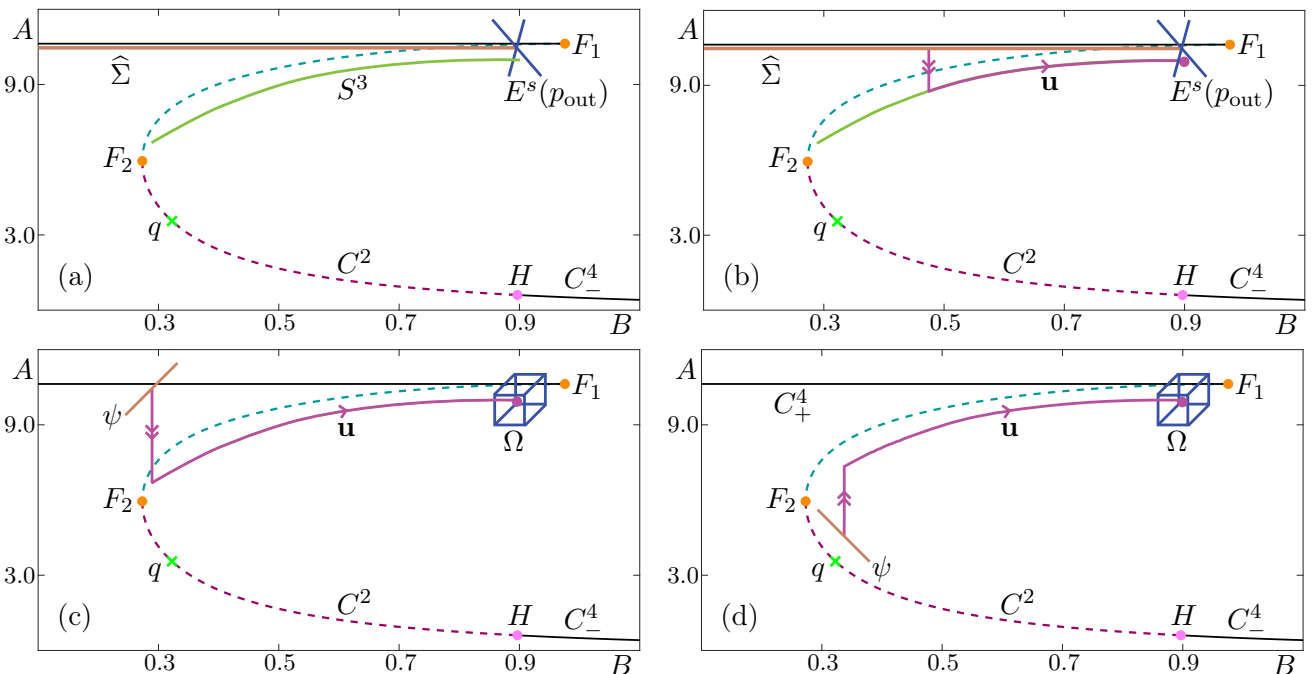


Fig. 3. A sketch in projection onto the  $(B, A)$ -plane of the numerical set-up for the computation of submanifolds of  $W^s(S^3)$ . Panel (a) shows a sketch at the start of the first homotopy step for computing  $W_\Sigma^s$  with  $S^3$  (a green curve),  $E^s(p_{\text{out}})$  (blue cross), and the plane  $\widehat{\Sigma}$  (mocha line) which is defined by the  $A$ - and  $Y$ -coordinates of the point  $p_{\text{out}}$ . Panel (b) shows a representative orbit segment  $\mathbf{u}$  (magenta curve) of the first homotopy step. Panel (c) shows an illustration of the selection of a  $\mathbf{u}$  (magenta curve) with maximal integration time that starts at  $\psi$  (mocha line) and ends on  $\Omega$  (blue cube) which is spanned by  $E^s(p_{\text{out}})$  and a vector in the  $B$ -direction; the one-dimensional subset  $\psi \subset \widehat{\Sigma}$  is defined by fixing  $B = B_{\text{in}}$ . Panel (d) shows a sketch of the selection of a different submanifold  $W_\Sigma^s$  for  $\Sigma$  on the other side of the critical manifold. Also shown are  $C^2$ ,  $C^3$ ,  $C_\pm^4$ ,  $F_1$ ,  $F_2$ ,  $H$  and  $q$ .

We compute the submanifold  $W_\Sigma^s$  as a one-parameter family of orbit segments  $\mathbf{u} = \{\mathbf{u}(s) \mid 0 \leq s \leq 1\}$  of the rescaled system

$$\frac{d\mathbf{u}}{ds} = TF(\mathbf{u}), \quad (4)$$

where  $\mathbf{u}(s) = (A(s), B(s), X(s), Y(s)) \in \mathbb{R}^4$  is the vector of chemical concentrations,  $F$  is the right-hand side of (1) and  $T$  is the total integration time on the fast timescale  $t = Ts$ . Orbit segments  $\mathbf{u} \in W_\Sigma^s$  must satisfy the boundary conditions

$$\mathbf{u}(0) \in \Sigma, \quad (5)$$

$$\mathbf{u}(1) \in \Omega = E^s(p_{out}) \times [0 \ 1 \ 0 \ 0]^{tr}, \quad (6)$$

and

$$T = T^B \quad (7)$$

where, for each  $B_p \in [B_{\text{in}}, B_{\text{out}}]$ ,  $T^B$  is the maximum integration time of an orbit segment with  $\mathbf{u}(0)_B = B_p$  satisfying (4) and (5). Conditions (5), (6) and (7) define four conditions that are satisfied by a one-parameter family of solutions to (4). Once an initial  $\mathbf{u}$  satisfying (4), (5), (6), and (7) is found, it is possible to sweep out the rest of  $W_\Sigma^s$  by continuing  $\mathbf{u}$  in  $T$ . The challenge then becomes the computation of an initial solution. For this purpose, we use homotopy steps as in [Farjami *et al.*, 2018; DesRoches *et al.*, 2009].

In the first homotopy step, we take the point  $p_{out} = (10.6055 \ 0.9 \ 0.0492484 \ 0.000230006) \in C^3$  and  $\Sigma = \Sigma_0 = \{\omega \in \mathbb{R} \mid \omega_A = 10.6055, \omega_Y = 0.000230006\}$ . Then  $\mathbf{u}(t) = p_{out}$  is a solution to (4), (5), and (6) with  $T = 0$ . In the second homotopy step, we obtain an orbit segment by increasing  $T$  until  $\mathbf{u}(0)$  is in a region where we can perform the third homotopy step of moving  $\Sigma$  to the desired location. In the final homotopy step, we fix  $\mathbf{u}(0)_B$  to ensure that an increase in integration time is the result of the slow segment's approach to  $S^3$  and not the result of decreasing  $\mathbf{u}(0)_B$ . Integration time  $T$  is increased until a local maximum is attained at which point we have found an initial  $\mathbf{u}$  with which we can sweep out the rest of  $W_\Sigma^s$ .

Figure 3 illustrates, step-by-step, the algorithm for computing  $W_\Sigma^s$  in projection onto  $(B, A)$ -space for the plane  $\Sigma$  given by constant values of  $A$  and  $X$  or  $Y$ . Each panel shows  $C$  from Figure 1 with additional information for the computation. For clarity, we move the line representing  $\Sigma_0$  so it is not confused with  $C_+^4$ . Panels 3(a)-(c) illustrate the set-up for obtaining a first solution on  $W_{\Sigma_0}^s$  via homotopy steps. We impose the condition (5), that is, we impose two restrictions on the startpoint  $\mathbf{u}(0)$  of the orbit segment  $\mathbf{u}$  because  $\Sigma_0$  is two dimensional. To find a unique  $\mathbf{u}$  satisfying (6) we require the more restrictive condition

$$\mathbf{u}(1) \in E^s(p_{out}), \quad (8)$$

that imposes two restrictions on  $\mathbf{u}(1)$  and allows for the possibility of  $\mathbf{u}(1)$  intersecting  $W^u(S^3)$ . The extra restriction of (8) ensures that our 2PBVP is well defined. Note that  $E^s(p_{out})$  is transverse to  $W^u(S^3)$ . In Figure 3(a)  $\Sigma_0$  is sketched as a mocha curve directly under  $C_+^4$ , intersecting  $E^s(p_{out})$  which is sketched as a blue cross. Note that by construction, the point  $p_{out}$  is a solution of the 2PBVP defined by (4), (5), and (8) with  $T = 0$ .

We increase the total integration time while allowing the  $B$ -value of  $\mathbf{u}(0)$  to decrease towards  $F_2$ . The continuation is stopped when  $\mathbf{u}(0)_B = B_{\text{in}} = 0.275$ . Figure 3(b) shows an intermediate orbit segment, a fast segment, followed by a slow segment along  $S^3$ . Panel (c) shows  $\mathbf{u}$  when the continuation is stopped, just before  $\mathbf{u}(0)_B$  reaches the  $B$ -coordinate value of  $F_2$ .

The orbit segment illustrated in Figure 3(c) belongs to a two-parameter family of solutions  $\mathbf{u}$  of (4) that satisfy the boundary conditions (5) and (6) for  $\Sigma = \Sigma_0$ . In the case where we would like to compute  $W_\Sigma^s$  for  $\Sigma$  defined by different constant values of  $A$  and  $Y$  (or  $X$ ) we perform additional homotopy steps to move  $\Sigma$ . Starting with an intermediate orbit segment from the first homotopy step, we impose (5) and (6) while keeping as free parameters  $T$  and  $\mathbf{u}(0)_B$ . In two runs, we continue  $\mathbf{u}$  while increasing or decreasing the  $A$ - and  $Y$ -values (or  $X$ -values) of  $\Sigma$  until we obtain the desired plane. We then decrease  $\mathbf{u}(0)_B$  and stop the continuation when  $\mathbf{u}(0)_B = B_{\text{in}}$ . Depending on  $\Sigma$ , the value of  $B_{\text{in}}$  may need to be increased to avoid running into  $C$ .

As mentioned before, we would like to find orbit segments with maximal integration time. To select a one-parameter family of orbit segments from those satisfying (5) and (6), we select for each  $B \in [B_{\text{in}}, B_{\text{out}}]$  the  $\mathbf{u}$  with maximal integration time such that  $\mathbf{u}(0)_B = B$ . In other words, we select a one-parameter family of  $\mathbf{u}$  that satisfy (7). We fix  $\mathbf{u}(0)_B$  to make sure an increase in integration time results from a better approximation of an orbit segment in  $W_\Sigma^s$ . To ensure that our 2PBVP is well defined with the extra restriction on  $\mathbf{u}(0)$ , we must allow an extra degree of freedom for  $\mathbf{u}(1)$ . To find an initial  $\mathbf{u}$  we fix  $\mathbf{u}(0)_B$  by requiring

$$\mathbf{u}(0) \in \psi = \Sigma_0 \cap \{\omega \in \mathbb{R}^4 \mid \omega_B = B_{\text{in}}\}, \quad (9)$$

which imposes three conditions on  $\mathbf{u}(0)$  and is more restrictive than (5). We then require (6) which imposes only one condition on  $\mathbf{u}(0)$ . Figures 3(c)-(d) show condition (6) as a blue cube labeled  $\Omega$  and condition (9) as a mocha line. Figure 3(c) illustrates the numerical setup for  $\Sigma = \Sigma_0$  while Figure 3(d) illustrates the numerical setup for a choice of  $\Sigma$  on the other side of  $C^3$  with respect to the variable  $A$ . We now track the solution  $\mathbf{u}$  of the 2PBVP (4), (6), and (9) as  $T$  increases, forcing  $\mathbf{u}(0)$  to approach  $W^s(S^3) \cap \Sigma$  and  $\mathbf{u}(1)$  to approach  $W^u(S^3) \cap \Omega$ . When a fold in  $T$  is reached, a (local) minimum in the total integration time  $T$  is attained.

The orbit segment that is obtained is the desired  $\mathbf{u}$  with maximal integration time. It is not represented in a figure because it is almost identical to the orbit segment illustrated in Figure 3(c): it begins in  $\Sigma$  and has a fast approach to  $S^3$  before remaining  $O(\varepsilon)$  close for  $O(1)$  slow time. By definition it is an orbit segment in  $W_\Sigma^s$ . In addition to finding an orbit segment that approximates a solution to (4) laying on  $W_\Sigma^s$ , we can approximate  $S^3$  by restricting the orbit segment further inside  $[B_{\text{in}}, B_{\text{out}}]$  to exclude fast segments. At this stage we use (5), (6), and (7) to sweep out a one-parameter family of solutions which gives an accurate approximation of  $W_\Sigma^s$ .

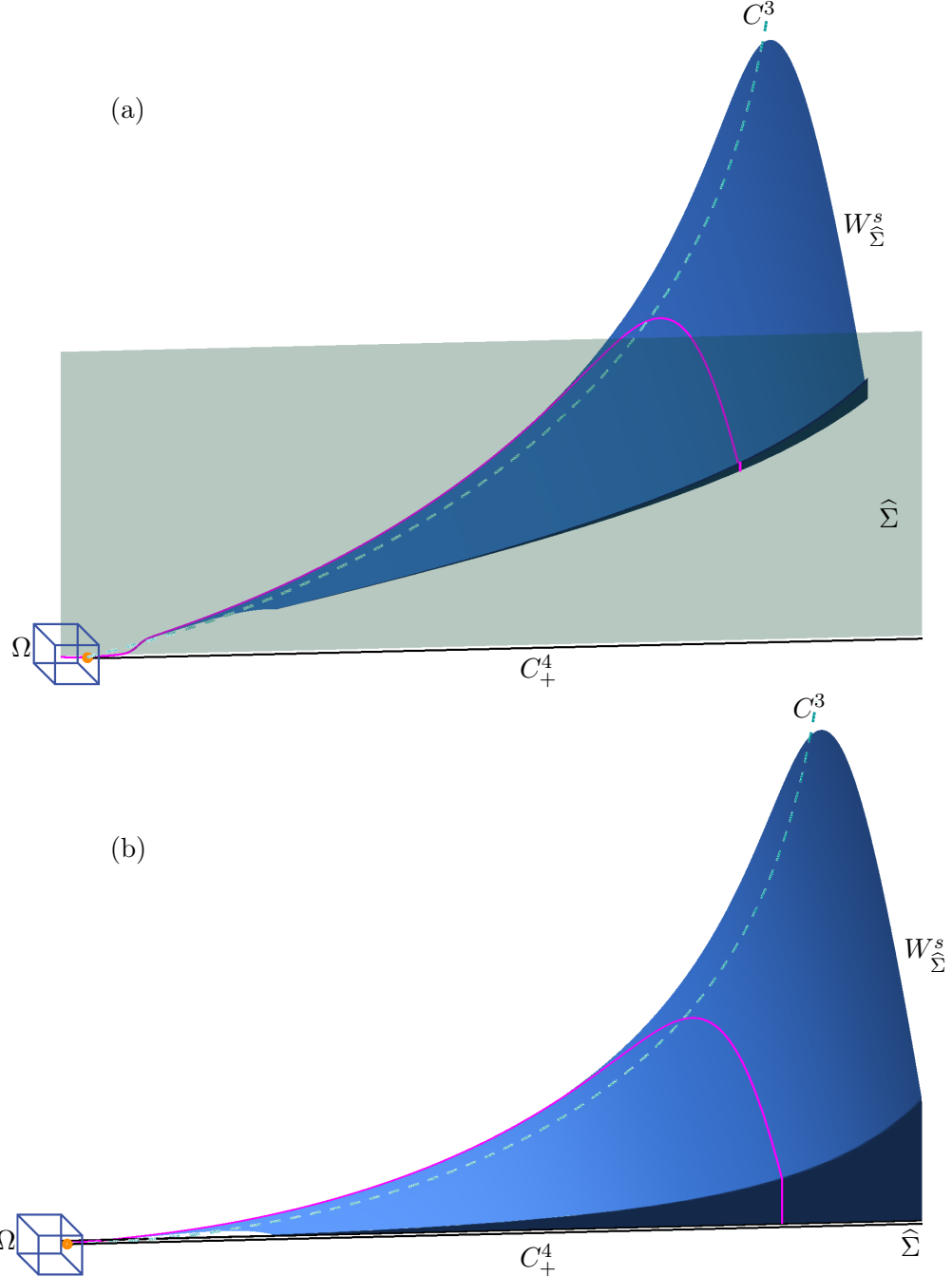


Fig. 4. The submanifold  $W_{\Sigma_0}^s$  (light blue surface) of  $W^s(S^3)$  shown in projection onto  $(B, A, X)$ -space (a) and onto  $(B, A, Y)$ -space (b); also shown are a representative orbit segment (magenta curve),  $\widehat{\Sigma}$  (mint surface and line),  $\Omega$  (represented by a blue cube),  $C^3$ ,  $C^4_+$ , and  $F_1$ .

Figure 4 shows  $W_{\Sigma_0}^s$  (light blue surface) in projection onto  $(B, A, X)$ -space and  $(B, A, Y)$ -space with  $\Sigma_0$  (mint surface). Although the manifold is two dimensional, it is necessary to visualise it in both  $(B, A, X)$ - and  $(B, A, Y)$ -projections because it exists in four-dimensional space. Lying on  $W_{\Sigma_0}^s$  is an orbit segment  $\mathbf{u}$  (magenta curve) representative of a trajectory in  $W_{\Sigma_0}^s$ . Orbits lying on  $W_{\Sigma_0}^s$  have a fast approach to  $S^3$  in  $X$  and  $Y$  before approaching mainly in the  $A$ -direction and then finally remaining close to  $C^3$  for  $O(1)$  slow time. Also shown are  $C^3$ ,  $C^4_+$ ,  $F_1$ , and  $\Omega$ . The view is rotated relative to earlier figures to help illustrate the geometry of the submanifold.

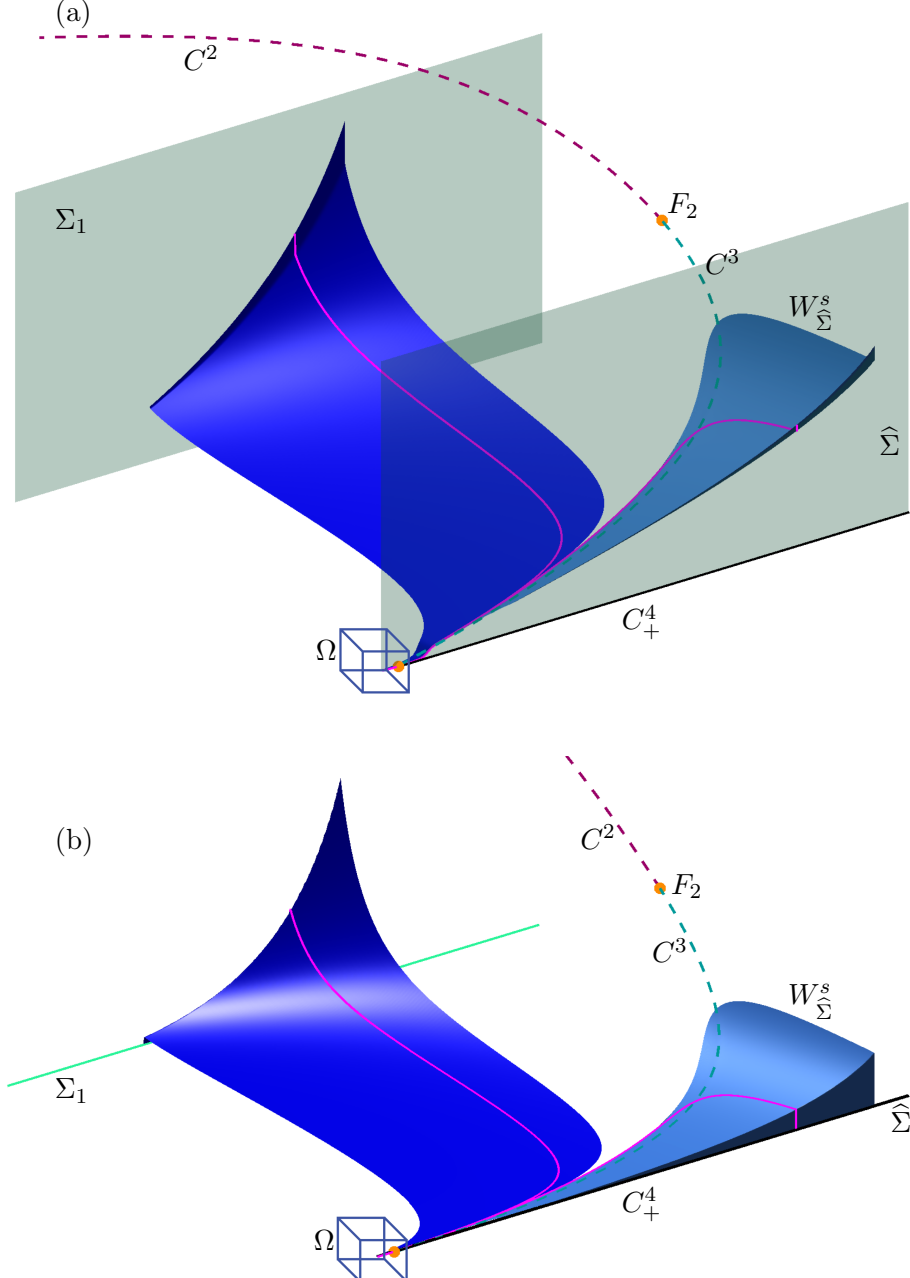


Fig. 5. The submanifolds  $W_{\Sigma_1}^s$  (blue surface) and  $W_{\widehat{\Sigma}}^s$  (light blue surface) of  $W^s(S^3)$  shown in projection onto  $(B, A, X)$ -space (a) and onto  $(B, A, Y)$ -space (b); also shown are representative orbit segments (magenta curves), planes  $\Sigma_0$  (mint surface and line) and  $\Sigma_1$  (mint surface and line), and  $\Omega$  (represented by a blue cube),  $C^2$ ,  $C^3$ ,  $C_+^4$ ,  $F_1$ , and  $F_2$ .

Figure 5 shows  $W_{\Sigma_0}^s$  (light blue surface) together with one other submanifold  $W_{\Sigma_1}^s$  (blue surface) of  $W^s(S^3)$  in projection onto  $(B, A, X)$ -space and  $(B, A, Y)$ -space, for  $\Sigma_1$  (mint surface) given by  $A = 2.0$  and  $Y = 0.0$ .

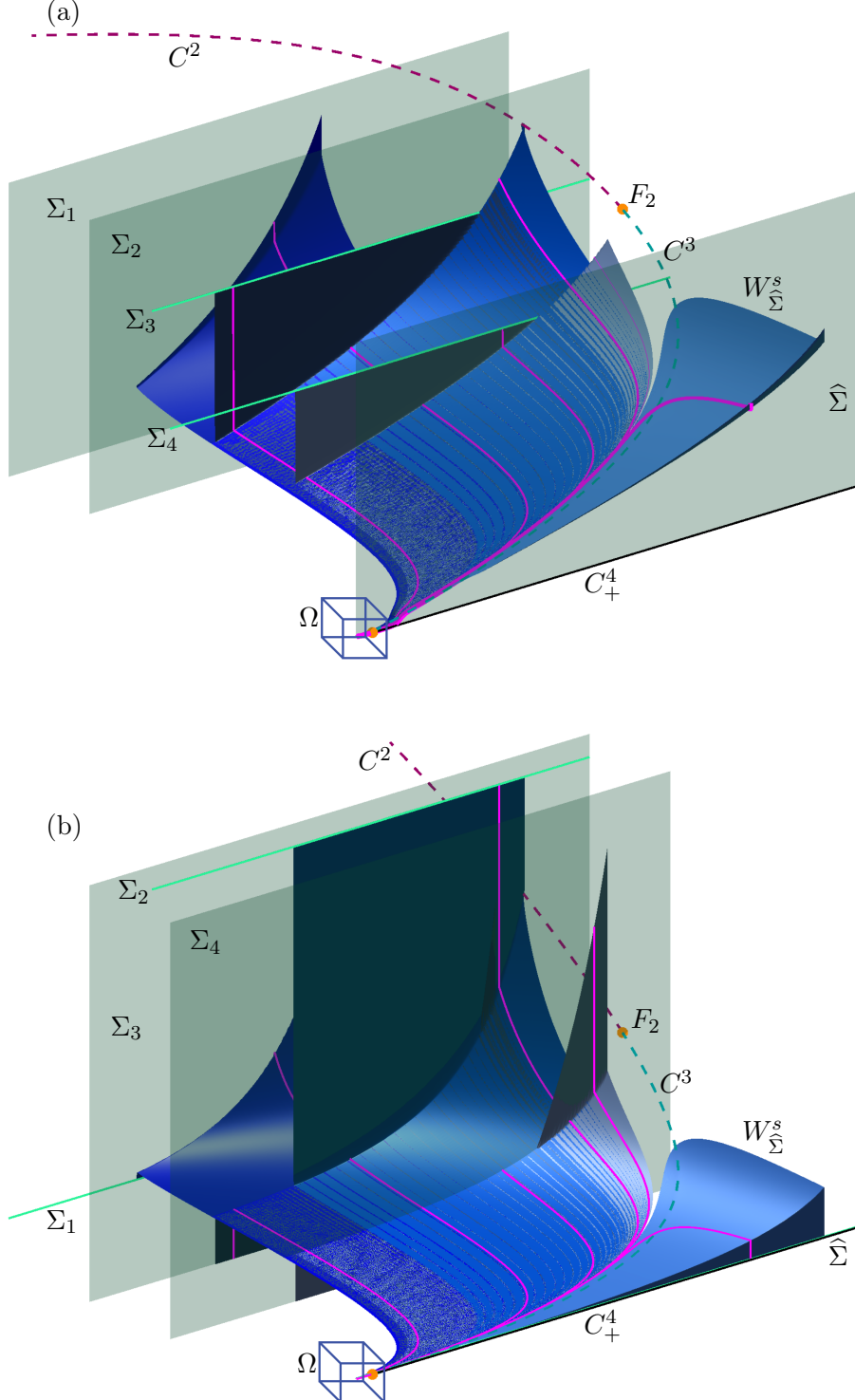


Fig. 6. The submanifolds from Figure 5 with three additional submanifolds  $W_{\Sigma_i}^s$  (blue surfaces) defined by  $\Sigma_2$ ,  $\Sigma_3$ , and  $\Sigma_4$  (mint planes and lines) shown in projection onto  $(B, A, X)$ -space (a) and onto  $(B, A, Y)$ -space (b); also shown are  $\Omega$  (represented by a blue cube). An example orbit segment (magenta curve) is plotted on each  $W_{\Sigma_i}^s$ . Also shown are  $C^2$ ,  $C^3$ ,  $C_+^4$ ,  $F_1$ , and  $F_2$ .

Figure 6 shows the two submanifolds of  $W^s$  shown in Figure 5 along with three additional submanifolds (blue surfaces) and the planes  $\Sigma_i$  (mint surfaces) that define them. Also shown are  $C^3$ ,  $C_+^4$ ,  $F_1$ , and  $\Omega$ . The additional submanifolds were selected with  $\Sigma_2$  given by  $A = 4.0$  and  $Y = 0.75$ ,  $\Sigma_3$  given by  $A = 4.0$

and  $X = 0.75$ , and  $\Sigma_4$  given by  $A = 6.0$  and  $X = 0.5$ . Note that each  $\Sigma$  appears as a line in one of the two projections, which projection depends on whether they are defined by constant values of  $X$  or  $Y$ .

The submanifolds appear to intersect in Figure 6, however this is due to the variable  $A$  being slower than variables  $X$  and  $Y$ . Orbit segments approach  $S^3$  in the  $X$ - and  $Y$ -directions before approaching in the  $A$ -direction. This is the responsible for the flat regions of the submanifolds that come very near to each other. Different choices of  $B_{\text{in}}$  and  $B_{\text{out}}$  also cause some submanifolds to extend farther than others in the  $B$ -direction.

We can reliably compute any number of submanifolds  $W_\Sigma^s$  with conditions (5), (6), and (7) and the homotopy steps outlined above. Together, these two-dimensional submanifolds give an understanding of the dynamics inside  $W^s(S^3)$ .

Unlike the stable manifold of  $S^3$  computed for the reduced system in [Desroches *et al.*, 2009], none of the  $W_\Sigma^s$  reach  $S^2$  in backward time, but rather diverge in the  $X$ - and  $Y$ - directions. The computations in [Desroches *et al.*, 2009] suggest that there exists a choice of  $\Sigma$  in (1) such that  $W_\Sigma^s$  spirals around  $S^2$  in backwards time. Such a  $W_\Sigma^s$  would be in the intersection of the two three-dimensional manifolds  $W^s(S^3)$  and  $W^u(S^2)$  in the full four-dimensional system.

### 3.3. Definition and computation of $W^u(S^2)$

Before investigating the existence of such an intersection, we first consider the unstable manifold  $W^u(S^2)$  of  $S^2$ . The computation of a submanifold of  $W^u(S^2)$  is similar to the computation of a  $W_\Sigma^s$ , however adjustments must be made in light of two complicating challenges. These are the saddle equilibrium  $q$  of the full system in  $C^2$  at  $B = 0.323$  and the Hopf bifurcation of the fast subsystem at  $B = 0.897$ . These are respectively shown as a green cross and a pink dot in Figures 1 and 3. Additional care must be taken to ensure that the computed orbits do not increase in integration time solely by approaching the saddle equilibrium's stable manifold or by following the stable slow manifold associated with  $C_+^4$  backward in time. Values for  $B_{\text{in}}$  and  $B_{\text{out}}$  are chosen such that  $q_B < B_{\text{out}} < B_{\text{in}} < H_B$ . We can then define the four-dimensional cylinder  $\mathcal{D}$  similarly to how it was defined for  $W^s(S^3)$ , substituting  $C^2$  for  $C^3$ . We consider a two-parameter family of orbit segments that enter  $\mathcal{D}$  at  $B_{\text{in}}$ , follow  $S^2$  for an  $O(1)$  amount of slow time and then exit at  $B_p$  for some  $B_p \in [B_{\text{in}}, B_{\text{out}}]$  and take the collection of fast, exiting segments of these to be  $W^u(S^2)$ . This is the same definition given for  $W^s(S^3)$  with the exception that we reverse the direction of time. We modify the steps for selecting and computing two-dimensional submanifolds of  $W^s(S^3)$  in order to ensure that an increase in integration time results only from a more accurate approximation of a submanifold of  $W^u(S^2)$ .

To select a submanifold of  $W^u(S^2)$ , we choose an  $r > \delta$  and for each  $B_p \in [B_{\text{in}}, B_{\text{out}}]$  define a two-dimensional sphere in the subspace  $\{B = B_p\}$ , centered at  $p$  and with radius  $r$ ; here  $p \in C^2$  is the unique point such that  $p_B = B_p$ . More formally,

$$\tilde{D}_r(B_p) = \{w \in \mathbb{R}^4 \mid w_B = B_p, \|w - p\| = r\}.$$

We can then define the three-dimensional cylinder  $\mathcal{R} = \cup_{B \in [B_{\text{in}}, B_{\text{out}}]} \tilde{D}_r(B)$ .

There is then a submanifold  $W_r^u$  for  $r > \delta$  consisting of a one-parameter family of orbit segments that enter  $\mathcal{D}$  at  $B_{\text{in}}$  and, for each  $B_p \in [B_{\text{in}}, B_{\text{out}}]$ , intersect  $\mathcal{R}$  after exiting  $\mathcal{D}$  at  $B_p$  an  $O(1)$  amount of slow time later. To ensure that our choice of  $W_r^u$  is unique, we require that orbit segments have maximal integration time for each  $B_p \in [B_{\text{in}}, B_{\text{out}}]$ . The radius  $r$  is chosen small enough so that  $\mathcal{R}$  does not contain a locus of points at which the flow is not transverse to  $\mathcal{R}$ . Using the cylinder  $\mathcal{R}$  instead of the plane  $\Sigma$  described in section 3.2 ensures that endpoints  $\mathbf{u}(1)$  remain close enough to  $C^2$  so that the  $\mathbf{u}$  cannot contain segments that approach  $q$ . In the following steps, the computation of a submanifold  $W_{r^*}^u$  is outlined for  $r^* = 0.7$ . We then describe the necessary modifications to obtain  $W_r^u$  for more general  $r$ .

We perform an initial homotopy step analogous to the first homotopy step in section 3.2 to obtain a first orbit segment that enters  $\mathcal{D}$  at  $B_{\text{in}}$  and intersects  $\mathcal{R}$  after exiting  $\mathcal{D}$  at some  $\tilde{B} \in [B_{\text{in}}, B_{\text{out}}]$ . We select the unique point  $\tilde{p} \in C^2$  such that  $\tilde{p}_B = 0.7$ . The plane  $\tilde{\Sigma}$  is defined by fixing the  $A$ - and  $Y$ - coordinates of  $\tilde{p}$ , which are  $A \approx 0.940272$  and  $Y \approx 1.342954$ . We impose the boundary conditions

$$\mathbf{u}(0) \in E^u(\tilde{p}), \quad (10)$$

and

$$\mathbf{u}(1) \in \tilde{\Sigma} \quad (11)$$

which each impose two conditions on  $\mathbf{u}(0)$  and  $\mathbf{u}(1)$ , respectively. The point  $\tilde{p}$  is then a solution to the 2PBVP defined by (4), (10), and (11) for  $T = 0$ . We increase  $T$  while  $\mathbf{u}(1)_B$  decreases and stop the continuation when  $\mathbf{u}(1)$  intersects  $\mathcal{R}$ . This step is almost identical to the initial homotopy step in section 3.2 except that we reverse the direction of time and instead of stopping the continuation when  $\mathbf{u}(1)_B$  attains a certain value, we stop the continuation when  $u(1)$  intersects  $\mathcal{R}$ . We denote by  $B_{\text{stop}}$  the  $B$ -value of  $\mathbf{u}(1)$  at the end of this step and  $p_{\text{stop}}$  the corresponding point in  $C^2$  such that  $p_{\text{stop}_B} = B_{\text{stop}}$ .

We perform a second homotopy step to ensure that  $\mathbf{u}(0)$  is such that  $\mathbf{u}$  comes close to  $S^2$  for  $O(1)$  slow, but cannot follow the attracting slow manifold for longer backward time. We define a three-dimensional space  $\Xi_{\text{HOM2}}$  spanned by  $E^u(\tilde{p})$  and a vector parallel to the  $B$ -direction. We also define a one-dimensional circle  $\Theta = \{w \in \mathbb{R}^4 \mid w_Y = \bar{p}_Y, w_B = B_{\text{stop}}, \|w - p^{\text{stop}}\| = 0.7\}$ . The orbit segment resulting from the first homotopy step is a solution to the 2PBVP defined by (4),

$$\mathbf{u}(0) \in \Xi_{\text{HOM2}}, \quad (12)$$

and

$$\mathbf{u}(1) \in \Theta. \quad (13)$$

Our goal is to continue the orbit segment by increasing  $T$  such that  $u(0)_B$  increases, that is (12) drives the continuation. Condition (13) is chosen so that our 2PBVP is well defined and integration time does not increase with decreasing  $\mathbf{u}(1)_B$ . The continuation is stopped when  $\mathbf{u}(0)_B = 1.0$ . The resulting orbit segment is initially attracted to the attracting slow manifold and follows it until it passes near  $\mathcal{H}$  at which point  $\mathbf{u}$  follows  $S^2$ . As following the attracting slow manifold for longer backwards time requires the increase of  $\mathbf{u}(0)_B$ , we fix  $\mathbf{u}(0)_B$  from this step onwards. This is different from section 3.2 in which  $\mathbf{u}(1)_B$  remains free in the final steps of the computation (recall that we consider negative  $T$  in section 3.2).

We define the plane  $\Phi = \{w \in \Xi_{\text{HOM2}} \mid w_B = 1.0\}$  and impose the boundary conditions

$$\mathbf{u}(0) \in \Phi, \quad (14)$$

and

$$\mathbf{u}(1) \in \{w \in \mathcal{R} \mid w_B = B_{\text{stop}}\}. \quad (15)$$

Condition (15) requires that  $\mathbf{u}(1)$  remain on a two-dimensional sphere as opposed to the one-dimensional curve  $\psi$  described for condition (9) in section 3.2. We allow this extra degree of freedom for  $\mathbf{u}(1)$  because keeping  $\mathbf{u}(0)_B$  fixed in condition (14) imposes an extra constraint compared to condition (??) in section 4.1. Our aim is to select a smooth, one-parameter family of orbit segments from the two-parameter family of orbit segments satisfying the 2PBVP defined by (4), (14), and (15). To this end, for each  $B_p \in [B_{\text{in}}, B_{\text{out}}]$ , we select from the one-parameter family of orbit segments exiting  $\mathcal{D}$  at  $B_p$  the orbit segment with maximal integration time. The orbit segment resulting from the second homotopy step satisfies (4), (14), and (15). To find an orbit segment with maximal integration time, we increase integration time again until a fold in  $T$  is detected. The resulting orbit segment satisfies the conditions for being in  $W_{r^*}^u$ . Finally to obtain the rest of the submanifold  $W_{r^*}^u$  we switch the endpoint boundary condition to

$$\mathbf{u}(1) \in \mathcal{R} \quad (16)$$

which imposes one condition on  $\mathbf{u}(1)$ . In two runs, the fold in  $T$  is continued until  $\mathbf{u}(0)_B = B_{\text{out}} = 0.35$  and then again until  $\mathbf{u}(0)_B = B_{\text{in}} = H_B$  to sweep out  $W_{r^*}^u$ .

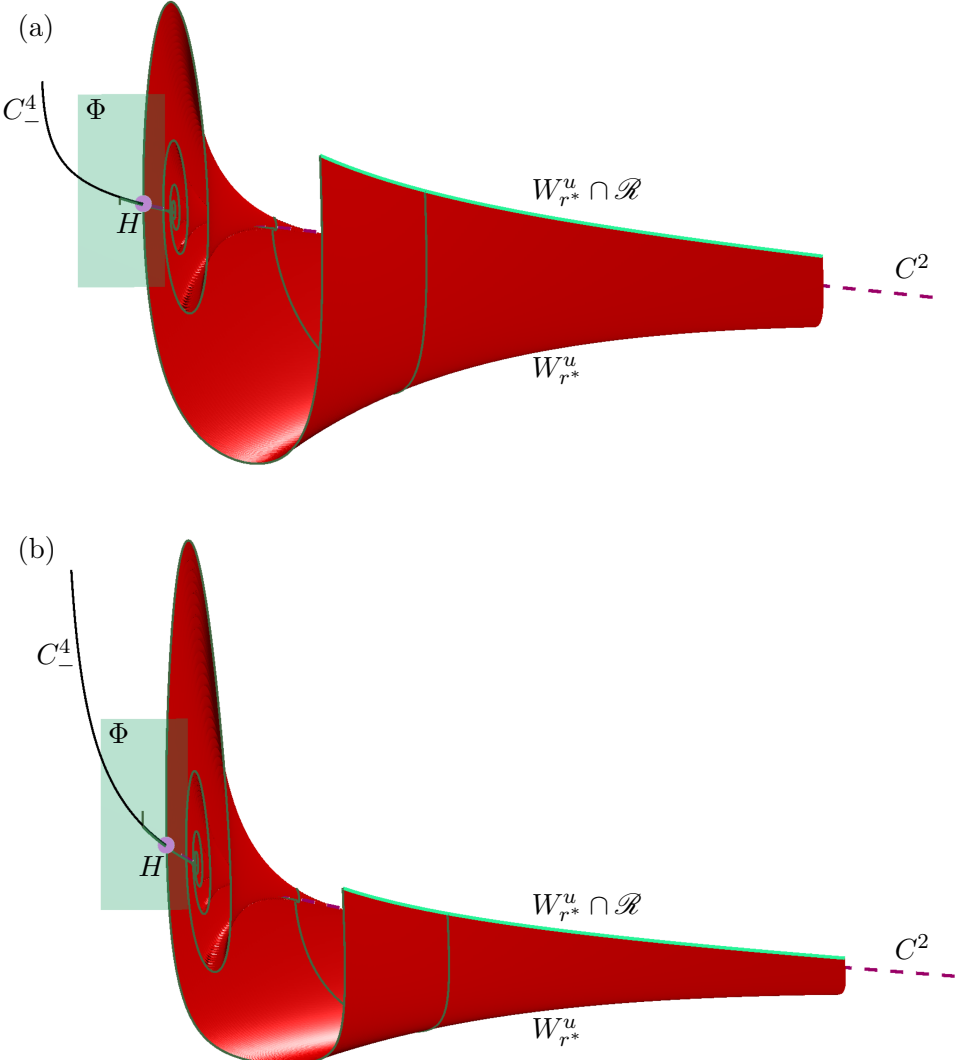


Fig. 7. The submanifold  $W_{r^*}^u$  (red surface) of  $W^u(S^2)$  shown in projection onto  $(B, A, X)$ -space (a) and  $(B, A, Y)$ -space (b); also shown are two representative orbit segments (forest green curves) on  $W_{r^*}^u$ ,  $\Phi$  (mint surface), and the intersection  $W_{r^*}^u \cap R$  (mint curve). Also shown are  $C^2$ ,  $C_-^4$ , and  $H$  and the view is rotated relative to previous figures.

Figure 7 shows two projections of the submanifold  $W_{r^*}^u$  (red surface) with  $W_{r^*}^u \cap R$  (mint curve) and  $\phi$  (mint surface). Note that  $W_{r^*}^u$  is simply the one-parameter family of  $\mathbf{u}(1)$ . Two example  $\mathbf{u}$  (forest green curves) are plotted and a subset of  $C^2$  (dashed raspberry curve) is shown. To facilitate viewing, the view is rotated relative to previous figures. From this angle, the radius of  $R$  may, to some readers, appear to decrease with decreasing  $\mathbf{u}(1)_B$ . This is due to the eye's erroneous association of points  $\mathbf{u}(1)$  with points  $p \in C^2$  such that  $p_B < \mathbf{u}(1)_B$ .

We can compute a different submanifold  $W_r^u$  by returning to the second homotopy step in our computation. Depending on the magnitude of  $r$ , we may need to perform one or two additional homotopy steps. In the case where  $r$  is large enough that  $\tilde{D}_r(\mathbf{u}(1)_B)$  contains a locus of points at which the flow is not transverse to it, two homotopy steps are needed after the second. We define a plane  $\Xi_{\text{hom3}}$  by fixing the  $A$ - and  $X$ -coordinates of  $\mathbf{u}(1)$  after the second homotopy step. To ensure that our 2PBVP is well defined, the orbit segment is continued with the boundary conditions (14) and

$$\mathbf{u}(1) \in \Xi_{\text{hom}3}, \quad (17)$$

which imposes two conditions on  $\mathbf{u}(1)$ . The endpoint  $B$ -coordinate  $\mathbf{u}(1)_B$  is increased until  $\tilde{D}_r(\mathbf{u}(1)_B)$  no longer contains a locus of tangent points. This step is not necessary if  $\tilde{D}_r(\mathbf{u}(1)_B)$  only contains points at which the flow is transverse to it.

The final homotopy step involves defining another plane  $\Xi_{\text{homfinal}}$  by fixing the  $B$ - and  $X$ -values of  $\mathbf{u}(1)$  after the second homotopy step, or the third homotopy step if a third homotopy step is necessary. Condition (14) is imposed while a new restriction

$$\mathbf{u}(1) \in \Xi_{\text{homfinal}}, \quad (18)$$

imposes two conditions on  $\mathbf{u}(1)$ . The radius  $r$  is then increased or decreased in the continuation until the desired value is attained. All that remains is to follow through with the rest of the steps to compute  $W_r^u$ . In the last step,  $B_{\text{out}}$  is chosen such that the flow is transverse to  $\tilde{D}(B_{\text{out}})$ . We do not show several submanifolds of  $W^u(S^2)$  in the same figure, because the spiralling dynamics near  $C^2$  make visualisation difficult in  $(B, A, X)$ -space and  $(B, A, Y)$ -space due to (self)-intersections of the submanifolds in these projections.

#### 4. A heteroclinic connection between two saddle slow manifolds

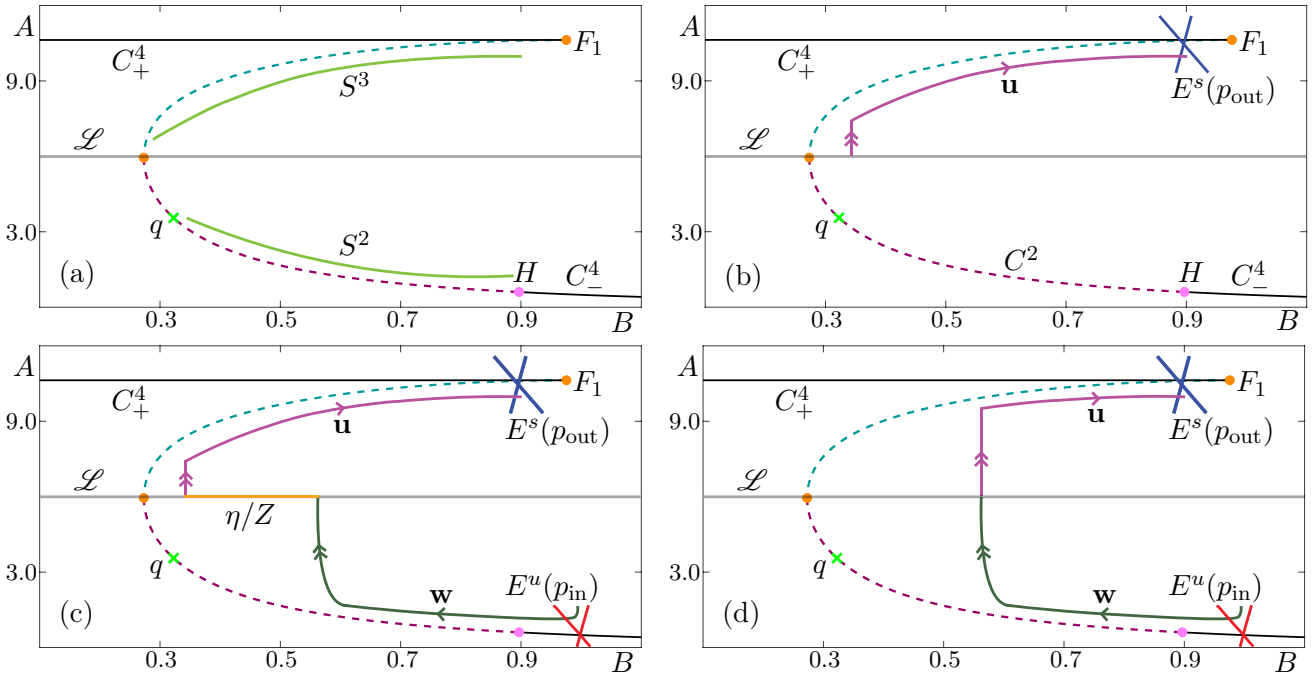


Fig. 8. Sketch of the numerical set up for the computation of  $\mathcal{H}$  with Lin's method in projection onto the  $(B, A)$ -plane. Panel (a) shows  $S^2$  and  $S^3$  (represented by green curves) and the Lin section  $\mathcal{L}$  (represented by a charcoal line). Panel (b) shows an initial orbit segment  $\mathbf{u} \in W^s(S^3)$  (represented by a magenta curve) such that  $\mathbf{u}(0) \in \mathcal{L}$  and  $\mathbf{u}(1) \in E^s(p_{\text{out}})$  (represented by a blue cross). Panel (c) additionally shows an initial orbit segment  $\mathbf{w} \in W^u(S^2)$  (represented by a forest green curve) such that  $\mathbf{w}(1) \in \mathcal{L}$  and  $\mathbf{w}(0) \in E^u(p_{\text{in}})$  (represented by a red cross). The points  $\mathbf{u}(0), \mathbf{w}(1)$  lie in the Lin space  $Z \subset \mathcal{L}$  (represented by a gold line) at a distance  $\eta$  (also represented by a gold line), called the Lin gap, from each other. Also shown are  $C^2$ ,  $C^3$ ,  $C_\pm^4$ ,  $F_1$ ,  $F_2$ , and  $H$ .

The generic intersection of the two three-dimensional manifolds  $W^s(S^3)$  and  $W^u(S^2)$  would be a two-dimensional manifold of heteroclinic connections in the four-dimensional phase space. We denote by  $\mathcal{H}$  the

surface of intersections to the right of  $W^u(q)$  with respect to the  $B$ -coordinate in the  $(B, A)$ -projection. We can compute such a surface of connections with an approach known as Lin's method [Lin, 1989; Krauskopf & Rieß, 2008; Zhang *et al.*, 2012]. Since Lin's method is typically used in parameter continuation of heteroclinic connections that are not structurally stable, we explain the set-up here for our context.

Figure 8 illustrates the set-up step-by-step. Panel (a) shows the critical manifold in projection onto  $(B, A)$ -space. The three-dimensional so-called Lin section  $\mathcal{L}$  (represented as a charcoal curve) is chosen so that it divides the four-dimensional phase space into two regions respectively containing  $S^3$  (represented as a green curve) and  $S^2$  (represented as a green curve) and so that, in the  $(B, A)$ -projection and with respect to the variable  $A$ , it lies between  $q$  and the point on  $C^3$  with the same  $B$ -coordinate as  $q$ . Our choice of  $\mathcal{L}$  allows us to avoid stopping the continuation because  $\mathcal{L}$  has intersected  $C^2$ . We can instead compute the largest possible portion of  $\mathcal{H}$  by continuing orbit segments as close as possible to  $q$ . In panel (b) we illustrate the computation of an orbit segment  $\mathbf{u}$  (represented as a magenta curve) lying on  $W^s(S^3)$  such that  $\mathbf{u}(0) \in \mathcal{L}$ . Panel (c) additionally shows a representation of an orbit segment  $\mathbf{w}$  (forest green curve) in  $W^u(S^2)$  such that  $\mathbf{w}(1) \in \mathcal{L}$ .

We define a vector  $\mathbf{v}_Z \in \mathbb{R}^4$  called a Lin vector and given by

$$\mathbf{v}_Z = \frac{\mathbf{u}(0) - \mathbf{w}(1)}{\|\mathbf{u}(0) - \mathbf{w}(1)\|} \quad (19)$$

as well as two unit normal vectors  $\mathbf{n}_1, \mathbf{n}_2 \in \mathcal{L}$  such that  $\mathbf{n}_i \perp \mathbf{v}_Z$  for  $i = 1, 2$  and  $\mathbf{n}_1 \perp \mathbf{n}_2$ . While our choice for the vector  $\mathbf{v}_Z$ , and normal vectors  $\mathbf{n}_1$  and  $\mathbf{n}_2$  is arbitrary, their selection remains fixed for the remainder of the computation. The span of  $\mathbf{v}_Z$  defines a one-dimensional space,  $Z \subset \mathcal{L}$ , called a Lin space and represented as a gold line in panel (c). The distance between  $\mathbf{u}(0)$  and  $\mathbf{w}(1)$  in  $Z$  defines the a Lin gap which is a regular test function denoted  $\eta$  and represented with the same gold line. We approximate an orbit segment on  $\mathcal{H}$  by continuation in the direction of decreasing  $\eta$  while requiring  $\mathbf{u}(0), \mathbf{w}(1) \in Z$ . When  $\eta = 0$ , an orbit segment on  $\mathcal{H}$  is detected as the concatenation of  $\mathbf{w}$  and  $\mathbf{u}$ .

In our computations of  $\mathbf{u}$  and  $\mathbf{w}$  we do not search for orbit segments with maximal integration time as it is not straightforward to track two folds simultaneously with the automatic fold continuation in the package AUTO [Doedel, 2007]. Since we are not requiring that  $\mathbf{w}$  satisfy the condition of maximal integration time, we do not run into the same issues encountered in section 3.3 for the computation of a submanifold of  $W^u(S^2)$ . For this reason we may compute  $\mathbf{w}$  in a manner more similar to the computation of  $\mathbf{u}$  in section 3.2.

#### 4.1. Computing an initial orbit segment on $W^s(S^3)$

We choose  $\mathcal{L} = \{\omega \in \mathbb{R}^4 \mid \omega_A = 6.0\}$  and compute the orbit segment  $\mathbf{u}$  as in the computation of an initial orbit segment on a submanifold  $W_\Sigma^s$  in section 3.2 with the exception that we choose  $B_{\text{out}} = 0.95$  and omit last the step of computing the orbit with maximal integration time. Here,  $\Sigma$  is the plane given by  $A = 6.0$  and  $Y = 3.5072 \times 10^{-5}$  which is the  $Y$ -coordinate of our new  $p_{\text{out}}$ .

#### 4.2. Computing an initial orbit segment on $W^u(S^2)$

We perform three homotopy steps to obtain an initial orbit segment on  $W^u(S^2)$ . We begin with the point  $\tilde{p}$  that is a solution to the 2PBVP defined by (4), (10), and (11) for  $T = 0$ . We obtain an orbit segment  $\mathbf{w}$  by imposing conditions (10) and (11) while increasing integration time. The continuation is stopped when  $\mathbf{w}(1)_B = 0.6$ .

We then impose (12) and (11) while additionally requiring  $\mathbf{w}(1)_B = 0.6$ . We continue  $\mathbf{w}$  while increasing integration time once more while  $\mathbf{w}(0)_B$  increases, and stop the continuation when  $\mathbf{w}(0)_B = 1.0$ .

In the third homotopy step, we impose (14) while keeping  $\mathbf{w}(1)_B$  and  $\mathbf{w}(1)_Y$  fixed. The  $A$ -coordinate of  $\mathbf{w}(1)$  increases as  $T$  is increased. The continuation is stopped when  $\mathbf{w}(1)_A = 6.0$ . In other words, we stop the continuation when  $\mathbf{w}(1) \in \mathcal{L}$ .

### 4.3. Closing the Lin gap

We are now in a position to define vectors  $\mathbf{v}_Z$ ,  $\mathbf{n}_1$ , and  $\mathbf{n}_2$ . We define  $\mathbf{v}_Z$  using the orbit segments  $\mathbf{u}$  and  $\mathbf{w}$  obtained in sections 4.1 and 4.2 and take  $\mathbf{n}_1 = (0, 0, \mathbf{v}_{Z_Y}, -\mathbf{v}_{Z_X})^{tr}$ , and  $\mathbf{n}_2 = (0, \mathbf{v}_{Z_Y}, 0, -\mathbf{v}_{Z_B})^{tr}$ . We

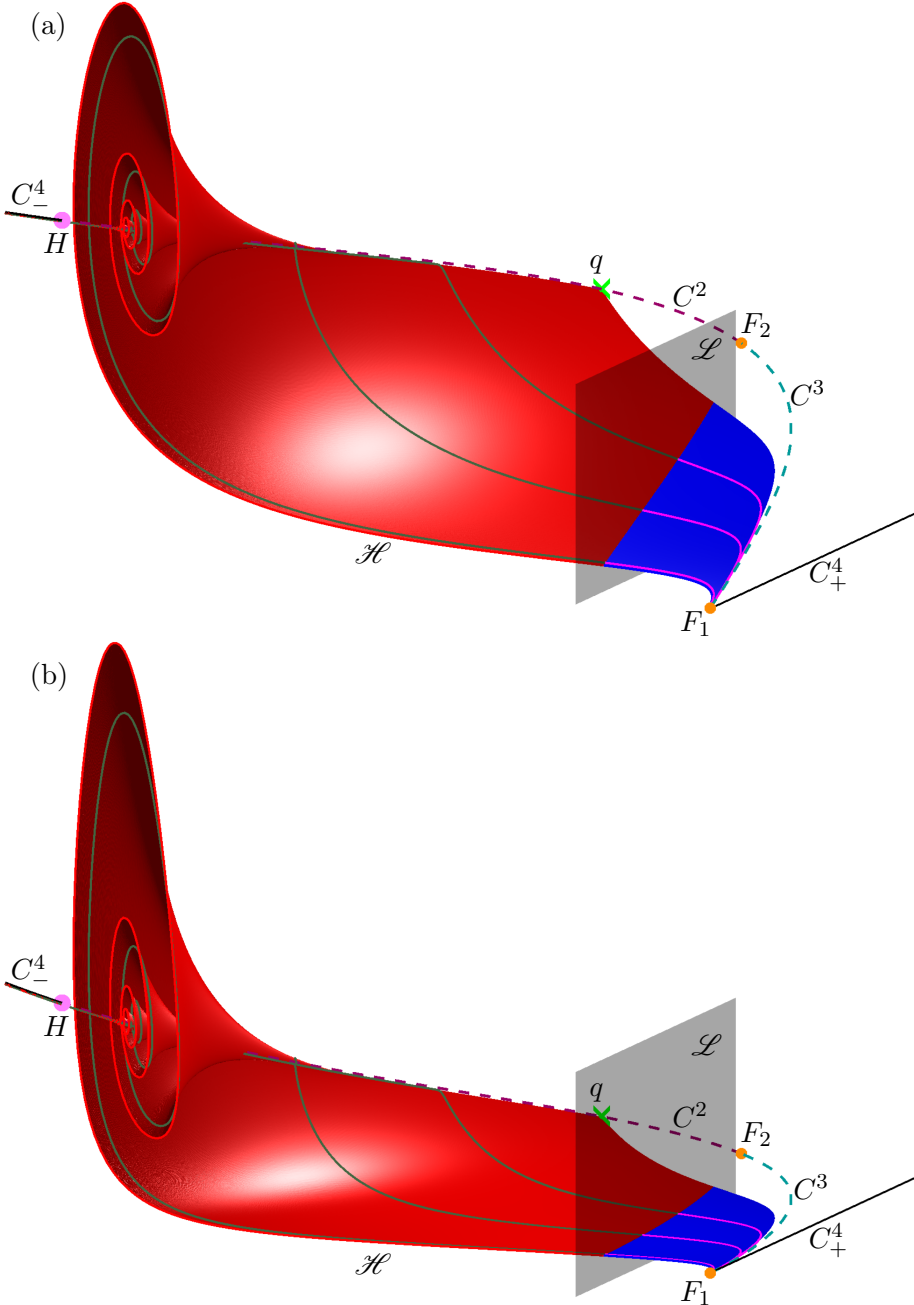


Fig. 9. The surface of heteroclinic connections  $\mathcal{H}$  (red/blue surface) and the Lin section  $\mathcal{L}$  (charcoal surface) in projection onto  $(B, A, X)$ -space (a) and onto  $(B, A, Y)$ -space (b). The part of  $\mathcal{H}$  that was computed as orbit segments in  $W^s(S^3)$  is plotted in blue while the part that was computed as orbit segments in  $W^u(S^3)$  is plotted in red. Also shown are three representative orbit segments on  $\mathcal{H}$ , where the  $\mathbf{u} \subset W^s(S^3)$  are magenta and the  $\mathbf{w} \subset W^u(S^3)$  are forest green. Notice the saddle equilibrium  $q \in C^2$  (green cross) which is partially obstructed by  $\mathcal{H}$  and  $\mathcal{L}$ . Also shown are  $C^2$ ,  $C^3$ ,  $C_\pm^4$ ,  $F_1$ ,  $F_2$ , and  $H$ .

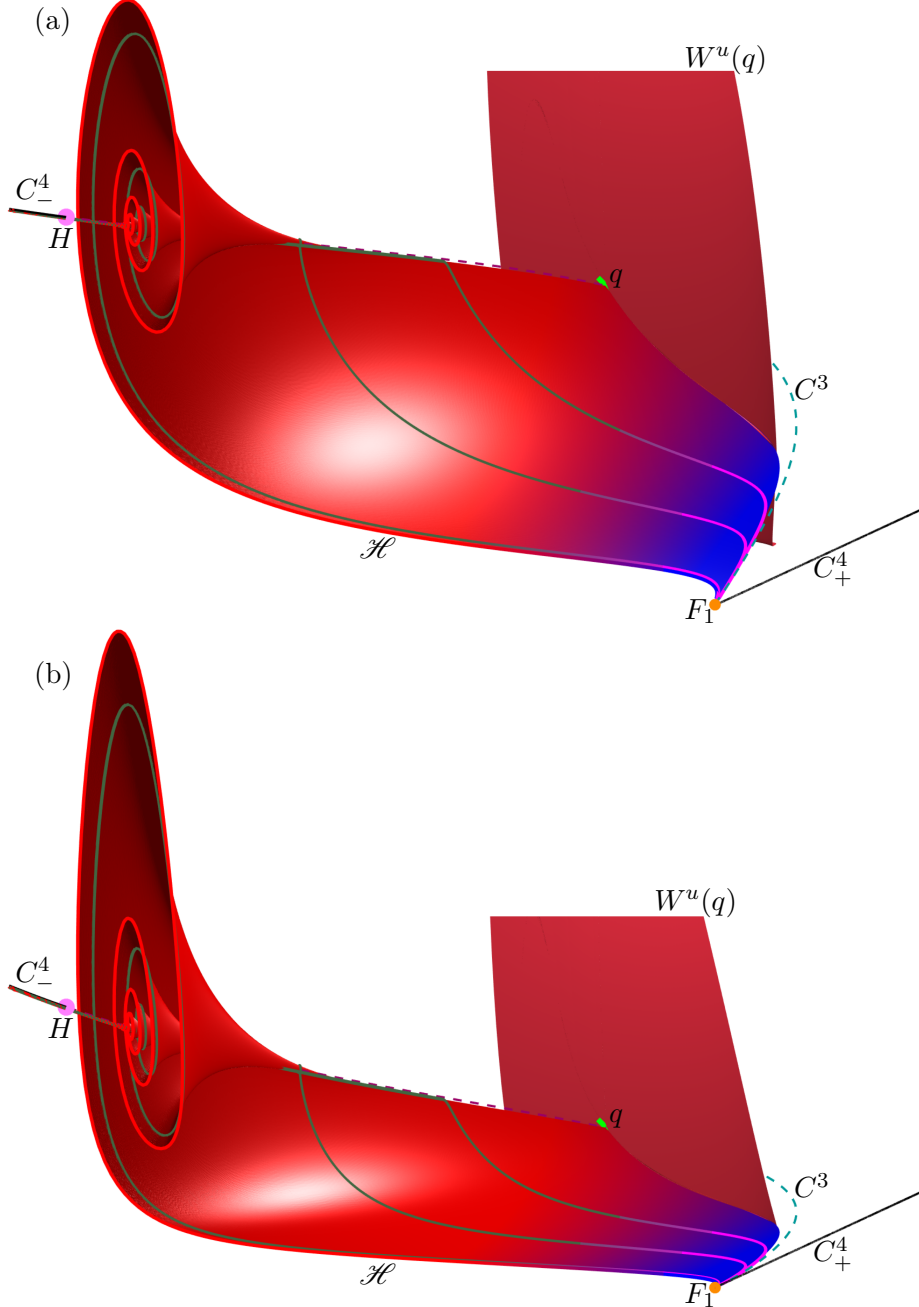


Fig. 10. The manifold  $W^u(q)$  (cardinal surface) is shown in projection onto  $(B, A, X)$ -space (a) and onto  $(B, A, Y)$ -space (b) and bounds the computed surface of heteroclinic connections  $\mathcal{H}$  (red-blue fade surface). The saddle equilibrium  $q$  (green cross) is partially obstructed by  $\mathcal{H}$  and  $W^u(q)$ ; compare with Figure 9. Also shown are  $C_-^4$ ,  $C^3$ ,  $C_+^4$ ,  $F_1$ ,  $F_2$ , and  $H$ .

impose conditions

$$\begin{aligned} \mathbf{u}(0), \mathbf{w}(1) &\in \mathcal{L}, \\ [\mathbf{u}(0) - \mathbf{w}(1)] \cdot \mathbf{n}_1 &= 0, \\ [\mathbf{u}(0) - \mathbf{w}(1)] \cdot \mathbf{n}_2 &= 0 \end{aligned} \tag{20}$$

to restrict  $[\mathbf{u}(0) - \mathbf{w}(1)] \in Z$  as illustrated in panel (c). Additionally, we impose conditions (??) and (14) while allowing the integration times of  $\mathbf{u}$  and  $\mathbf{w}$  to move freely. As illustrated in panel (c), the pair of orbit

segments  $\mathbf{u}$  and  $\mathbf{w}$  obtained at the end of section 4.2 are one of a two-parameter family of orbit-segment pairs satisfying (??), (14), and (20). To formulate a well-defined 2PBVP, we impose the restriction

$$\mathbf{w}(1)_B \in \{\omega \in \mathbb{R}^4 \mid \omega_B = 0.6\}, \quad (21)$$

and continue  $\mathbf{u}$  and  $\mathbf{w}$  while  $\eta$  is decreased. We stop the continuation as soon as  $\eta = 0$ , at which point the concatenation of  $\mathbf{w}$  with  $\mathbf{u}$  forms an approximation of a heteroclinic connection in  $\mathcal{H}$ .

To obtain a one-parameter family of concatenations approximating  $\mathcal{H}$ , we require  $\eta = 0$  while relaxing condition (21). We then decrease  $\mathbf{w}(1)_B$  and stop the continuation before  $\mathbf{u}$  and  $\mathbf{w}$  reach the intersection of  $\mathcal{H}$  with  $W^u(q)$ . We sweep out the other side of the manifold by continuation in the opposite direction (of increasing  $\mathbf{w}(1)_B$ ) and stop just before  $\mathbf{w}(1)_B$  reaches the  $B$ -coordinate of the Hopf bifurcation point  $H$  on  $C^2$ .

Figure 9 shows  $\mathcal{H}$  in projection onto  $(B, A, X)$ -space and  $(B, A, Y)$ -space with  $\mathcal{L}$  (charcoal surface). The surface of heteroclinic connections  $\mathcal{H}$  is divided by  $\mathcal{L}$  into a region composed of  $\mathbf{w}$  (red surface) and a region composed of  $\mathbf{u}$  (blue surface). Three representative orbit segments are shown as concatenations of  $\mathbf{w}$  (forest green curves) with  $\mathbf{u}$  (magenta curves). Orbit segments on  $\mathcal{H}$  spiral around and follow  $S^2$  for an  $O(1)$  amount of slow time and then traverse the region between  $C^2$  and  $C^3$  to follow  $S^3$  for an  $O(1)$  amount of slow time.

Figure 10 shows  $\mathcal{H}$  (red-blue fade surface) in projection onto  $(B, A, X)$ -space and  $(B, A, X)$ -space with the two-dimensional  $W^u(q)$  (cardinal surface). The unstable manifold  $W^u(q)$  is shown bounding  $\mathcal{H}$ , preventing us from computing the entire surface of heteroclinic connections. It partially obstructs the saddle equilibrium  $q$  (green cross) in the view shown. Three representative orbit segments (forest green-magenta fade curves) are also shown originating from  $S^2$  before traversing  $\mathcal{H}$  to  $S^3$ .

## 5. Computing the singular surface of heteroclinic connections

We compute the the singular surface analogous to  $\mathcal{H}$ , denoted  $\mathcal{H}_0$ , in the interest of analysing its interactions with MMOs for varying  $\varepsilon$ . The computation of  $\mathcal{H}_0$  for  $\varepsilon = 0$  is slightly different from the computation of  $\mathcal{H}$  for  $\varepsilon > 0$ . The time scaling parameter,  $\varepsilon$ , being zero means that  $\mathcal{H}_0 = W^s(C^3) \cap W^u(C^2)$ . The surface  $\mathcal{H}_0$  is then composed of the unique family of heteroclinic connections between saddle equilibria of (2) which is parameterized by  $B$ .

An additional challenge of computing  $\mathcal{H}_0$  is that equilibria of (2) in  $C^2$  are not all of the same type. In  $(B, A)$ -space, the equilibria in  $C^2$  to the left of  $B \approx 0.476858$  with respect to the  $B$ -coordinate have all real eigenvectors. Equilibria in  $C^2$  to the right have a complex conjugate pair of eigenvectors. Due to the change in the type of eigenvectors of equilibria on  $C^2$ , we compute  $\mathcal{H}_0$  in two pieces with two slightly different algorithms. We first describe the computation for equilibria with real eigenvectors and then for equilibria with complex conjugate eigenvectors.

For both computations, we consider solutions to the rescaled system

$$\frac{d\mathbf{u}}{ds} = TG(\mathbf{u}), \quad (22)$$

where  $\mathbf{u}(s) = (A(s), X(s), Y(s)) \in \mathbb{R}^3$  is the vector of chemical concentrations,  $G$  is the right hand side of (2), and  $T$  is integration time on the fast timescale  $t = Ts$ . The Lin section  $\mathcal{L}$  is taken to be the two-dimensional plane defined by a constant  $A = 6.0$ . Note that in the layer equation,  $\mathcal{L}$  is two dimensional and  $B$  is a parameter.

### 5.1. Real eigenvalues

For the first three steps of the computation, the parameter  $B$  is kept constant at a value of 0.4. We compute an initial orbit segment on  $W^s(C^3)$  following the algorithm for computing a two-dimensional global manifold as a solution family of BVPs outlined in [Krauskopf *et al.*, 2007]. We consider the equilibrium  $\tilde{p}_{\mathfrak{R}}$  of (2) for  $B = 0.4$  such that  $(\tilde{p}_{\mathfrak{R}_A}, 0.4, \tilde{p}_{\mathfrak{R}_X}, \tilde{p}_{\mathfrak{R}_Y}) \in C^3$ . We define a two-dimensional plane  $\tilde{\Sigma}_{\mathfrak{R}} = \{\omega \in \mathbb{R}^3 \mid \omega_Y =$

$\tilde{p}_{\Re} + r_{\Re} \mathbf{v}_{2Y}$ } and a one-dimensional circle  $\tilde{\Gamma}_{\Re} = \{\omega \in \mathbb{R}^3 \mid \tilde{p}_{\Re} + r_{\Re}(\mathbf{v}_1 \sin(\theta) + \mathbf{v}_2 \cos(\theta)), \theta \in [0, 2\pi]\}$  where  $r_{\Re} = 0.0001$  and  $\mathbf{v}_1$  and  $\mathbf{v}_2$  are the stable eigenvectors of  $\tilde{p}_{\Re}$ . The radius  $r_{\Re}$  of  $\tilde{\Gamma}_{\Re}$  is chosen small enough that  $\tilde{\Gamma}_{\Re}$  approximates a curve lying on  $W^s(\tilde{p}_{\Re})$  and large enough that AUTO can distinguish points on  $\tilde{\Gamma}_{\Re}$  from  $\tilde{p}_{\Re}$  itself. The point  $\tilde{p}_{\Re} + r_{\Re} \mathbf{v}_2$  is then a solution to the 2PBVP defined by (22) and the conditions

$$\mathbf{u}(1) \in \tilde{\Gamma}_{\Re}, \quad (23)$$

and

$$\mathbf{u}(0) \in \tilde{\Sigma}_{\Re} \quad (24)$$

for  $T = 0$ . An initial orbit segment  $\mathbf{u}$  on  $W^s(C^3)$  with start point in  $\mathcal{L}$  is obtained by decreasing  $\mathbf{u}(0)_A$  while allowing integration time to increase in backwards time, corresponding to negative  $T$ . The continuation is stopped when  $\mathbf{u}(0) \in \mathcal{L}$ , in other words, when  $\mathbf{u}(0)_A = 6.0$ .

In the second step, we obtain an initial orbit segment on  $W^u(C^2)$  with end point in  $\mathcal{L}$  through almost identical means. We consider the equilibrium  $\hat{p}_{\Re}$  of (2) for  $B = 0.4$  such that  $(\hat{p}_{\Re_A}, 0.4, \hat{p}_{\Re_X}, \hat{p}_{\Re_Y}) \in C^2$  and its unstable eigenvectors  $\mathbf{k}_1$  and  $\mathbf{k}_2$ . We then define a two-dimensional plane  $\hat{\Sigma}_{\Re} = \{\omega \in \mathbb{R}^3 \mid \omega_Y = \hat{p}_{\Re_Y} + r_{\Re} \mathbf{k}_{2Y}\}$  and a one-dimensional circle  $\hat{\Gamma}_{\Re} = \{\omega \in \mathbb{R}^3 \mid \hat{p}_{\Re} + r_{\Re}(\mathbf{k}_1 \sin(\theta) + \mathbf{k}_2 \cos(\theta)), \theta \in [0, 2\pi]\}$ . The point  $\hat{p}_{\Re} + r_{\Re} \mathbf{k}_2$  is then a solution to the 2PBVP defined by (22) and the conditions

$$\mathbf{w}(0) \in \hat{\Gamma}_{\Re} \quad (25)$$

and

$$\mathbf{w}(1) \in \hat{\Sigma}_{\Re}, \quad (26)$$

for  $T = 0$ . We increase  $\mathbf{w}(1)_A$  while also allowing integration time to increase in forward time, corresponding to positive  $T$ . The continuation is stopped when  $\mathbf{w}(1) \in \mathcal{L}$ .

In the third step, we define the Lin vector

$$\mathbf{v}_Z = \frac{\mathbf{u}(0) - \mathbf{w}(1)}{\|\mathbf{u}(0) - \mathbf{w}(1)\|}, \quad (27)$$

which is three dimensional. We also define a normal vector  $\mathbf{n} = (0, -\mathbf{v}_{Z_Y}, -\mathbf{v}_{Z_X})$  such that  $\mathbf{n} \perp \mathbf{v}_Z$ . We then impose the conditions

$$\begin{aligned} \mathbf{u}(0), \mathbf{w}(1) &\in \mathcal{L} \\ (\mathbf{u}(0) - \mathbf{w}(1)) \cdot \mathbf{n} &= 0, \end{aligned} \quad (28)$$

to restrict  $[\mathbf{u}(0) - \mathbf{w}(1)] \in Z$ , the space spanned by  $\mathbf{v}_Z$ . To close the Lin gap,  $\eta$  we impose conditions (23), (25), and (28) while decreasing  $\eta$  and allowing integration time to move freely. The continuation is stopped when  $\eta = 0$  at which point the concatenation of  $\mathbf{w}$  with  $\mathbf{u}$  forms an approximation of a heteroclinic connection on  $\mathcal{H}_0$ . We can then sweep out the portion of  $\mathcal{H}_0$  corresponding to real eigenvalues increasing and decreasing the parameter  $B$  inside the interval  $(F_{2B}, 0.47685750162]$  while requiring that  $\eta = 0$ . We choose to stop our continuation at  $B = 0.47685750162$ , before the eigenvalues switch from real to complex conjugate. Unlike the computation of  $\mathcal{H}$ , the computational set up for  $\mathcal{H}_0$  allows us to decrease  $B$  past the value of  $q_B$ . We are thus able to compute the entire portion of  $\mathcal{H}_0$  corresponding to real eigenvalues.

### 5.2. Complex conjugate eigenvalues

The method for computing an initial orbit segment  $\mathbf{u}$  in  $W^s(C^3)$  for complex conjugate eigenvalues is identical to the computation for real eigenvalues except that we choose  $B = 0.7$  instead of  $B = 0.4$  and consider the saddle equilibrium  $\tilde{p}_{\mathfrak{S}}$  of (2) such that  $(\tilde{p}_{\mathfrak{S}_A}, 0.7, \tilde{p}_{\mathfrak{S}_X}, \tilde{p}_{\mathfrak{S}_Y}) \in C^3$ . We choose  $\mathcal{L}$  again to be the two-dimensional plane given by  $A = 6.0$ .

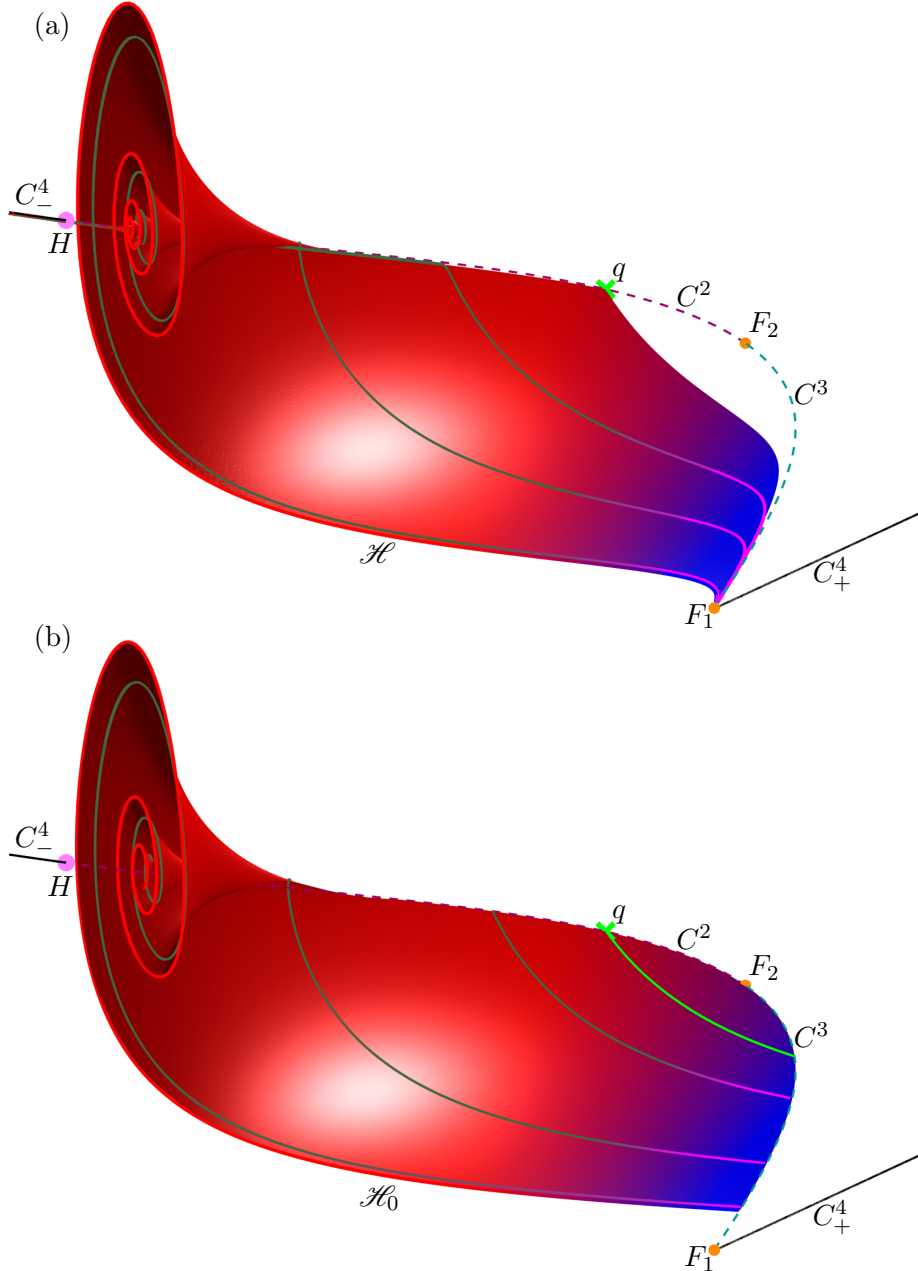


Fig. 11. Projections onto  $(B, A, X)$ -space of  $\mathcal{H}$  (red-blue fade surface) (a) and of the portion of  $\mathcal{H}_0$  (red-blue fade surface) lying in the region  $B < 0.781$  (b) with representative orbit segments (forest green-magenta fade curves). Also shown are the intersection  $W^u(q) \cap \mathcal{H}_0$  (green curve) for  $\varepsilon = 0$ ,  $q$ ,  $C^2$ ,  $C^3$ ,  $C_{\pm}^4$ ,  $F_1$ ,  $F_2$ , and  $H$ .

The computation of orbit segments on  $W^u(C^2)$  for complex conjugate eigenvalues presents an additional challenge. Some orbit segments on  $W^u(C^2)$  contain a segment that spirals tightly around  $C^2$  while others do not. Orbit segments that spiral tightly require larger mesh sizes than those that do not, however

mesh size is held constant in our continuation. To address this issue, we define a radius  $r_{\mathfrak{I}} = r_{\mathfrak{I}}(B)$ , where  $r_{\mathfrak{I}}(B)$  is the linear function such that  $r_{\mathfrak{I}}(0.47685750164) = 0.0001$  and  $r_{\mathfrak{I}}(0.86) = 0.2$ . By choosing a start point farther away from  $C^2$  in regions where orbit segments spiral tightly, we avoid computing those tightly spiralling pieces of the orbit segments.

We consider the equilibrium  $\hat{p}_{\mathfrak{I}}$  of (2) for  $B = 0.7$  such that  $(\hat{p}_{\mathfrak{I}A}, 0.7, \hat{p}_{\mathfrak{I}X}, \hat{p}_{\mathfrak{I}Y}) \in C^2$ . We define a two-dimensional plane  $\widehat{\Sigma}_{\mathfrak{I}} = \{\omega \in \mathbb{R}^3 \mid \omega_Y = \hat{p}_{\mathfrak{I}Y} + r_{\mathfrak{I}}(0.7)\mathbf{h}_{2Y}\}$  and a one-dimensional circle  $\widehat{\Gamma}_{\mathfrak{I}} = \{\omega \in \mathbb{R}^3 \mid \hat{p}_{\mathfrak{I}} + r_{\mathfrak{I}}(0.7)(\mathbf{h}_1 \sin(\theta) + \mathbf{h}_2 \cos(\theta)), \theta \in [0, 2\pi]\}$  where  $\mathbf{h}_1$  and  $\mathbf{h}_2$  are the real and complex parts of the unstable complex conjugate eigenvectors of  $\hat{p}_{\mathfrak{I}}$ . The point  $\hat{p}_{\mathfrak{I}} + r_{\mathfrak{I}}(0.7)\mathbf{h}_2$  then becomes a solution to the 2PBVP defined by (22) and the boundary conditions

$$\mathbf{w}(0) \in \widehat{\Gamma}_{\mathfrak{I}} \quad (29)$$

and

$$\mathbf{w}(1) \in \widehat{\Sigma}_{\mathfrak{I}}, \quad (30)$$

for  $T = 0$ . To obtain a  $\mathbf{w}$  such that  $\mathbf{w}(1) \in \mathcal{L}$ , we increase  $\mathbf{w}(1)_A$  while allowing  $T$  to increase and stop the continuation when  $\mathbf{w}(1)_A = 6.0$ .

We close the Lin gap by imposing the conditions (23), (28), and (29) while decreasing  $\eta$  and allowing integration time to move freely. The continuation is stopped when  $\eta = 0$  at which point the concatenation of  $\mathbf{w}$  with  $\mathbf{u}$  forms an approximation of a heteroclinic connection on  $\mathcal{H}_0$ . We can then sweep out the portion of the manifold corresponding to complex conjugate eigenvalues by increasing and decreasing the parameter  $B$  inside the interval  $[0.47685750164, H]$  while requiring that  $\eta = 0$ . We choose to stop the continuation at  $B = 0.47685750164$  before the eigenvalues switch from complex conjugate to real.

In Figure 11 we compare  $\mathcal{H}$  (red-blue fade surface) (a) and  $\mathcal{H}_0$  (red-blue fade surface) (b) in projection onto  $(B, A, X)$ -space. In panel (a), for visual comparison with  $\mathcal{H}$ , we show only the portion of  $\mathcal{H}_0$  that lies in the region  $B < 0.781$ . In panels (a) and (b), three representative orbit segments are shown in each surface (forest green-magenta fade curves). Unlike orbit segments in  $\mathcal{H}$ , orbit segments in  $\mathcal{H}_0$  do not exhibit any drift in the direction parallel to the  $B$ -axis. Also shown in Figure 11 are  $C^2$ ,  $C^3$ ,  $C_{\pm}^4$ ,  $F_1$ ,  $F_2$ , and  $H$ . The intersection of  $\mathcal{H}_0$  with the singular  $W^u(q)$  (green curve) is analogous to the border of  $\mathcal{H}$  near  $q$ . The border of  $\mathcal{H}_0$  near  $H$  also does contain segments that spiral as tightly as the border of  $\mathcal{H}$  near  $H$ . This is due to our requirement that orbit segments on  $\mathcal{H}_0$  remain farther away from  $C^2$  in this region to avoid numerical difficulties.

### 5.3. Distance from $\mathcal{H}_0$

We analyse the difference between  $\mathcal{H}$  and  $\mathcal{H}_0$  using the integral norm to measure the distance between intersection curves of  $\mathcal{H}$  and  $\mathcal{H}_0$  with different subspaces of the phase space defined by constant values of  $B$ .

## 6. Implications for mixed-mode oscillation geometry

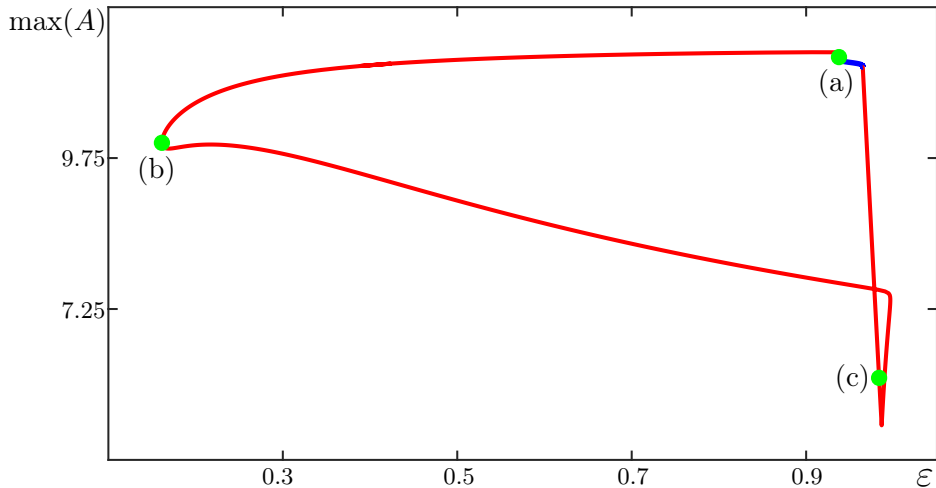


Fig. 12. The isola of MMO  $\Gamma$  over  $\varepsilon$ . The PO  $\Gamma$  is stable along the blue part and unstable along the red part of the isola. Green dots labeled (a), (b), and (c) correspond to  $\Gamma$  as shown in Figure 14.

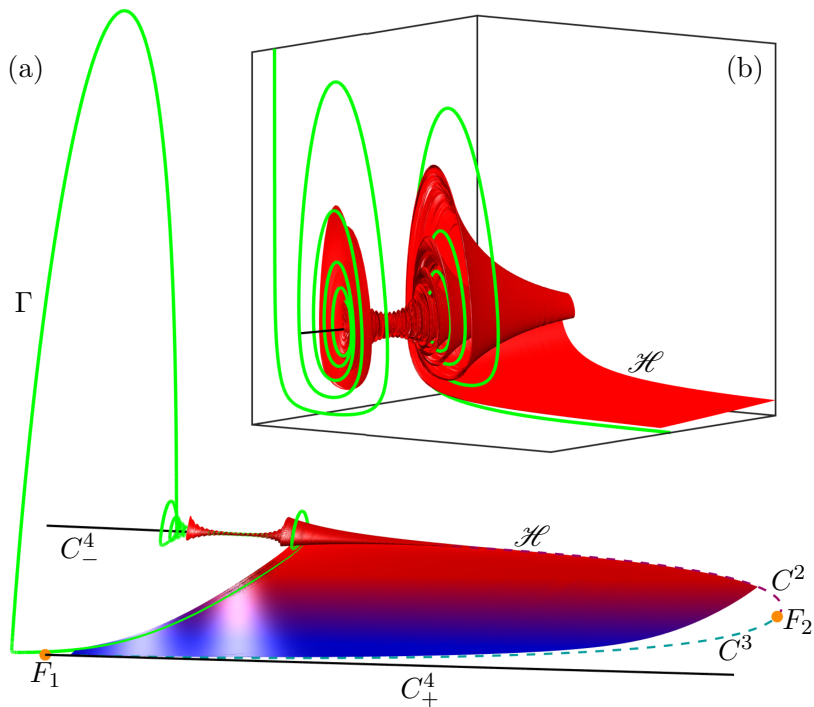


Fig. 13. The MMO  $\Gamma$  (green curve) and the surface of heteroclinic connections  $\mathcal{H}$  (red-blue fade) extended in backwards time past the Hopf bifurcation point  $H$  are shown in projection onto  $(B, A, X)$ -space. Panel (a) shows the global view of  $\Gamma$  tracking  $\mathcal{H}$  from  $C^2$  to  $C^3$  and making a LAO to  $C_+^4$ . Panel (b) shows the subsequent slow passage of  $\Gamma$  through  $H$ . Also shown are  $q$ ,  $C^2$ ,  $C^3$ ,  $C_\pm^4$ ,  $F_1$ ,  $F_2$ , and  $H$ .

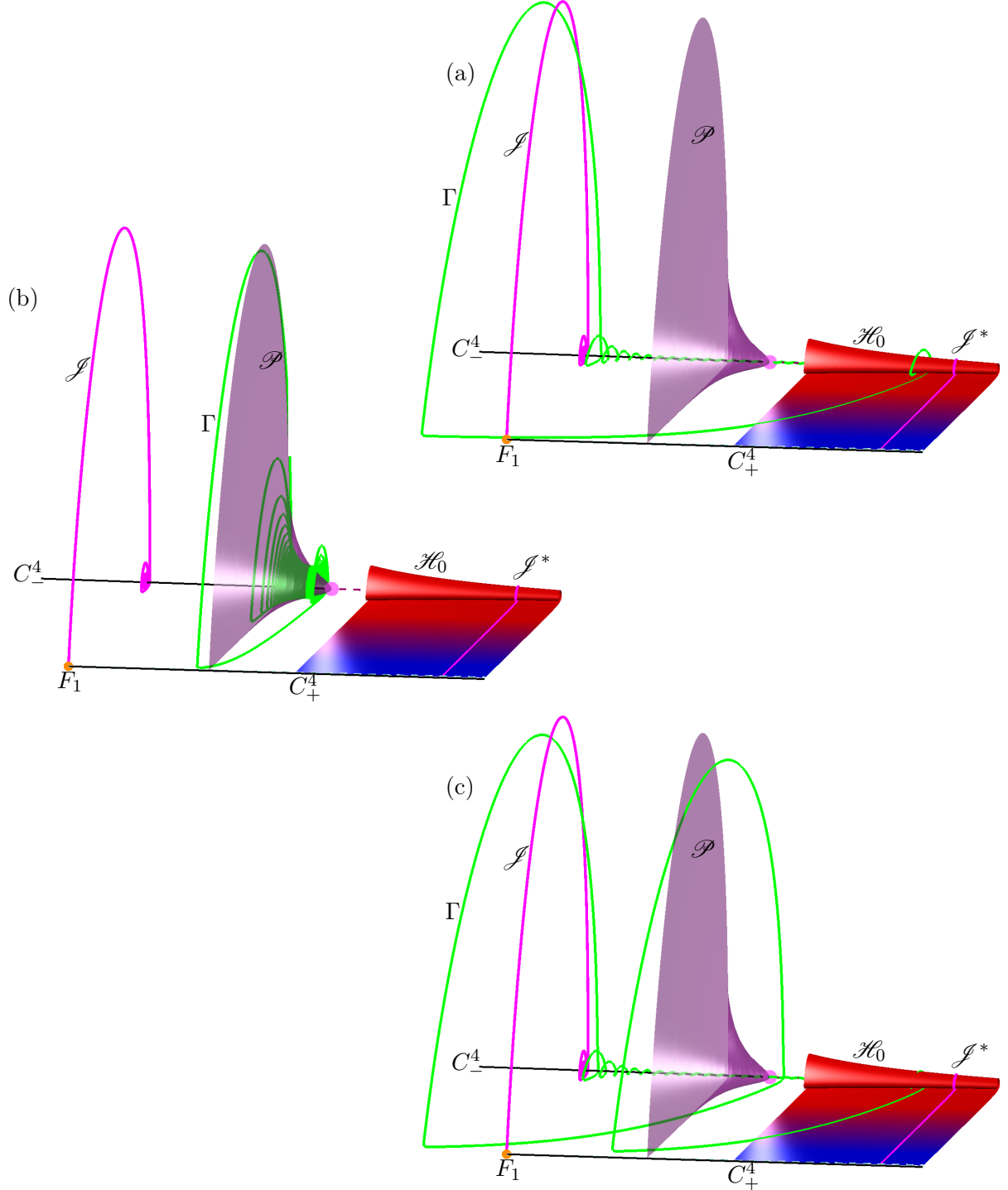


Fig. 14. Projections onto  $(B, A, X)$ -space of the portion of  $\mathcal{H}_0$  (red-blue fade surface) lying in the region  $B < 0.781$ , of the jump back trajectory  $\mathcal{J}$  (magenta curve) and its dual  $\mathcal{J}^*$  (magenta curve), and of the surface of singular PEs  $\mathcal{P}$  (midnight grape surface). Also shown are  $C^2$ ,  $C^3$ ,  $C_{\pm}^4$ ,  $F_1$ ,  $F_2$ , and  $H$ . Panel (a) shows  $\Gamma$  (green curve) for the original value of  $\varepsilon$ . The entry and exit of  $\Gamma$  into the region of SAOs are near  $\mathcal{J}$  and  $\mathcal{J}^*$ , respectively. Panel (b) shows a representative  $\Gamma$  (green curve) that remains near  $\mathcal{P}$ . Panel (c) shows a representative  $\Gamma$  (green curve) that has two LAOs. Entry and exits into the region of SAOs are again near  $\mathcal{J}$  and  $\mathcal{J}^*$ , respectively.

Figure 12 shows the isola (red and blue curve) of the MMO  $\Gamma$  over the time scaling parameter  $\varepsilon$ . The red segment of the isola indicates where  $\Gamma$  has at least one unstable Floquet multiplier and the blue

segment indicates where  $\Gamma$  is stable. Green dots labeled (a), (b), and (c) refer to panels of Figure 14. Only the green dot labeled (a) corresponds to stable  $\Gamma$ . Green dots labeled (b) and (c) correspond to  $\Gamma$  that have at least one unstable Floquet multiplier.

Figure 13 shows  $\Gamma$  (green curve) for the original value  $\varepsilon = 0.0037$  in projection onto  $(B, A, X)$ -space with  $\mathcal{H}$  (red-blue fade surface) which is extended in backwards time past  $H$ . Also shown are  $q$ ,  $C^2$ ,  $C^3$ ,  $C_\pm^4$ ,  $F_1$ ,  $F_2$ , and  $H$ . The MMO corresponds to the green dot in Figure 12 labeled (a) on the stable segment of the isola. Figure 13(a) shows the global view of  $\Gamma$ . We observe  $\Gamma$  entering into the region of SAOs near the stable branch  $C_-^4$  of  $C$ . The MMO spirals as it enters the scroll-like region of  $\mathcal{H}$  and makes a slow passage through the Hopf point  $H$  to  $S^2$ . An enlargement of  $\Gamma$ 's entry into the scrolls of  $\mathcal{H}$  (red surface) and its slow passage through  $H$  are shown in inlay (b). In the enlargement, we also see  $\Gamma$  exit the region of SAOs by spiralling out of the scrolls of  $\mathcal{H}$  to the underside of the flatter region of  $\mathcal{H}$ . In the global view (a), we observe  $\Gamma$  subsequently tracking an orbit segment in this flatter area of  $\mathcal{H}$ . The MMO travels into the blue region of  $\mathcal{H}$  before following  $S^3$ . Near  $F_1$ ,  $\Gamma$  falls off  $S^3$  and makes a single LAO back to the attracting slow manifold near  $C_-^4$ .

Figure 14 shows  $\mathcal{H}_0$  (red-blue fade surface) and several objects of system (2) with the full system MMO  $\Gamma$  in projection onto  $(B, A, X)$ -space. Panels (a), (b), and (c) respectively show  $\Gamma$  for values of  $\varepsilon$  corresponding to green dots labeled (a), (b), and (c) in Figure 12. Also shown are segments of  $C^3$ ,  $C^2$ , and  $C_-^4$  with  $F_1$  and  $H$ . A jump back trajectory  $\mathcal{J}$  (magenta curve) connects  $F_1$  to the equilibrium of (2) in  $C_-^4$  corresponding to  $B = F_{1B}$ . The jump back trajectory's dual  $\mathcal{J}^* \in \mathcal{H}_0$  (magenta curve) lies on the other side of and at an equal distance away from  $H$ . A surface of singular POs  $\mathcal{P}$  (midnight grape surface) for varying  $\varepsilon$  forms a cone that originates from  $H$  and terminates in a homoclinic connection of a saddle of (2) in  $C^3$ . Panel (a) shows  $\Gamma$  for the original value of  $\varepsilon = 0.0037$ . The LAO after  $\Gamma$  passes  $F_1$  can be seen tracking  $\mathcal{J}$  into the region of SAOs. We can easily see the passage of  $\Gamma$  through the Hopf point  $H$ , compare with Figure 13. As  $\Gamma$  passes through  $H$ , we observe it spiralling through the interior of  $\mathcal{P}$ . The MMO's exit out of the region of LAOs occurs near  $\mathcal{J}^*$ . Drift in the  $B$ -direction causes  $\Gamma$  to distances itself from  $\mathcal{J}^*$  on its way to  $C^3$ . Panel (b) shows  $\Gamma$  for  $\varepsilon = 0.0005$ . The MMO makes an LAO to the region of SAOs via the homoclinic connection at the widest end of  $\mathcal{P}$ . The SAOs of  $\Gamma$  track  $\mathcal{P}$ , but do not pass through  $H$ . Rather,  $\Gamma$  leaves  $C_-^4$  before reaching  $C^3$ , passing through  $\mathcal{P}$  in the  $(B, A, X)$ -projection. When  $\Gamma$  is away from  $C$ , we see less drift of  $\Gamma$  in the  $B$ -direction due to the smaller value of  $\varepsilon$ , compare with panel (a). Panel (c) shows  $\Gamma$  for  $\varepsilon = 0.0038$  which has two LAOs. For this value of  $\varepsilon$ ,  $\Gamma$  enters and exits the region of SAOs near  $\mathcal{J}$  and  $\mathcal{J}^*$  respectively. An early LAO back to  $C^2$  occurs between exit and reentry into the region of SAOs.

An animation of the change in  $\Gamma$ 's geometry for varying  $\varepsilon$  can be found in the supplementary materials. In this animation, we see the  $\Gamma$  shown in Figure 14(a) morphing smoothly into the  $\Gamma$  shown in Figure 14(b). We then see the  $\Gamma$  shown in Figure 14(b) morphing into the  $\Gamma$  shown in Figure 14(c). Finally, we see the  $\Gamma$  shown in Figure 14(c) morph back into the  $\Gamma$  shown in Figure 14(a). The green dot shown in the inlay tracks the location of  $\Gamma$  around the isola from figure 12.

## References

- Benoît, E. [1982] “Systèmes lents-rapides dans  $\mathbb{R}^3$  et leurs canards,” *Proceedings of the Third Schnepfenried Geometry Conference* **2**, 159–191.
- Benoît, E. [1985] “Enlacements de canards,” *Comptes Rendus Mathematique Academie des Sciences* **300**, 225–230.
- Benoît, E., Callot, J. F., Diener, F. & Diener, M. [1981] “Chasse au canard,” *Collectanea Mathematica* **31**, 37–119.
- Brøns, M. & Bar-Eli, K. [1991] “Canard explosion and excitation in a model of the Belousov-Zhabotinskii reaction,” *Journal of Physical Chemistry A* **95**, 8706–8713.
- Brøns, M., Krupa, M. & Wechselberger, M. [2006] “Mixed mode oscillations due to the generalized canard phenomenon,” *Fields Institute Communications* , 39–63.
- De Maesschalck, P. & Wechselberger, M. [2015] “Neural Excitability and Singular Bifurcations.” *The Journal of Mathematical Neuroscience* **5**.
- Desroches, M., Guckenheimer, J., Krauskopf, B., Kuehn, C., Osinga, H. & Wechselberger, M. [2012] “Mixed-Mode Oscillations with Multiple Time Scales.” *SIAM Review* **54**, 211–288.
- DesRoches, M., Krauskopf, B. & Osinga, H. [2009] *Elements of Applied Bifurcation Theory*, 2nd ed. (Springer International Publishing).
- Desroches, M., Krauskopf, B. & Osinga, H. [2009] “The geometry of mixed-mode oscillations in the Olsen model for peroxidase-oxidase reaction.” *Discrete & Continuous Dynamical Systems* **2**, 807–827.
- Doedel, E. [2007] *AUTO-07p: Continuation and Bifurcation Software for Ordinary Differential Equations*, URL <http://indy.cs.concordia.ca/auto/>, with major contributions from A.R. Champneys, F. Dercole, T.F. Fairgrieve, Y.A. Kuznetsov, R.C. Paffenroth, B. Sandstede, X. Wang and C. Zhang.
- Farjami, S., Kirk, V. & Osinga, H. [2018] “Computing the Stable Manifold of a Saddle Slow Manifold.” *SIAM Journal on Applied Dynamical Systems* **17**, 350–379.
- Fenichel, N. [1979] “Geometric singular perturbation theory for ordinary differential equations,” *Journal of Differential Equations* **31**, 53–98.
- FitzHugh, R. [1955] “Mathematical models of threshold phenomena in the nerve membrane,” *The bulletin of mathematical biophysics* **17**, 257–278.
- Guckenheimer, J. [1985] “Singular hopf bifurcation in systems with two slow variables,” *SIAM Journal on Applied Dynamical Systems* **7**, 1355–1377.
- Háro, A. & de la Liave, R. [2006] “A parameterization method for the computation of invariant tori and their whiskers in quasi-periodic maps: Rigorous results,” *Journal of Differential Equations* **228**, 530–579.
- Harvey, E., Kirk, V., Osinga, H., Sneyd, J. & Wechselberger, M. [2010] “Understanding anomalous delays in a model of intracellular calcium dynamics,” *Chaos: An Interdisciplinary Journal of Nonlinear Science* **20**.
- Hasan, C., Krauskopf, B. & Osinga, H. [2018] “Saddle slow manifolds and canard orbits in  $\mathbb{R}^4$  and application to the full Hodgkin-Huxley model,” *Journal of Mathematical Neuroscience* **8**.
- Hudson, J. L., Hart, M. & Marinko, D. [1979] “An experimental study of multiple peak periodic and nonperiodic oscillations in the Belousov-Zhabotinskii reaction,” *The Journal of Chemical Physics* **71**, 1601–1606.
- Jorba, A. & Olmedo, E. [2009] “On the computation of reducible invariant tori on a parallel computer,” *SIAM Journal on Applied Mathematics* **8**, 1382–1404.
- Krauskopf, B., Osinga, H. & Galán-Vioque [2007] *Numerical continuation methods for dynamical systems* (Springer International Publishing).
- Krauskopf, B. & Rieß, T. [2008] “A lin’s method approach to finding and continuing heteroclinic connections involving periodic orbits,” *Nonlinearity* **21**, 1655–1690.
- Krupa, M., Popović, N. & Kopell, N. [2008] “Mixed-mode oscillations in three time-scale systems: A prototypical example,” *SIAM Journal on Applied Dynamical Systems* , 361–420.
- Kuehn, C. & Szmolyan, P. [2015] “Multiscale Geometry of the Olsen Model and Non-classical Relaxation Oscillations.” *Journal of Nonlinear Science* **25**, 583–629.

- Kuznetsov, Y. A. [2009] *Elements of Applied Bifurcation Theory*, 2nd ed. (Springer International Publishing).
- Lin, X. [1989] “Shadowing lemma and singularly perturbed boundary value problems,” *SIAM Journal of Applied Mathematics* **49**, 26–54.
- Mitry, J., McCarthy, M., Kopell, N. & Wechselberger, M. [2013] “Excitable neurons, firing threshold manifolds and canards,” *The journal of mathematical neuroscience* **3**.
- Olsen, L. [1983] “An enzyme reaction with a strange attractor.” *Physics Letters A* **94**, 454–457.
- Otto, C., Ludge, K., Vladimirov, A. G., Wolfrum, M. & Scholl, E. [2012] “Delay-induced dynamics and jitter reduction of passively mode-locked semiconductor lasers subject to optical feedback,” *New Journal of Physics* **14**.
- Piltz, S. H., Veerman, F., Maini, P. K. & Porter, M. A. [2017] “A predator–2 prey fast–slow dynamical system for rapid predator evolution,” *SIAM Journal on Applied Dynamical Systems* **16**, 54–90.
- Rockafellar, R. T. & Wets, R. J.-B. [2009] *Variational Analysis*, 3rd ed. (Springer International Publishing).
- Van der Pol, B. [1927] “Forced oscillations in a circuit with non-linear resistance. (Reception with reactive triode).” *The London, Edinburgh, and Dublin Philosophical Magazine and Journal of Science* **3**, 65–80.
- Vo, T., Bertram, R. & Wechselberger, M. [2013a] “Multiple geometric viewpoints of mixed mode dynamics associated with pseudo-plateau bursting,” *SIAM Journal on Applied Dynamical Systems* **12**.
- Vo, T., Tabak, J., Bertram, R. & Wechselberger, M. [2013b] “A geometric understanding of how fast activating potassium channels promote bursting in pituitary cells,” *Journal of Computational Neuroscience* **36**.
- Waalkens, H., Burbanks, A. & Wiggins, S. [2005] “A formula to compute the microcanonical volume of reactive initial conditions in transition state theory,” *Journal of Physics A: Mathematical and General* **38**, L759–L768, URL <http://stacks.iop.org/0305-4470/38/i=45/a=L03>.
- Zhang, W., Krauskopf, B. & Kirk, V. [2012] “How to find a codimension-one heteroclinic cycle between two periodic orbits,” *Discrete and Continuous Dynamical Systems* **32**, 2825–2851.